

HiMAP: Hilbert Mass-Aligned Parameterization for Multivariate Barycenters and Fréchet Regression

Tao Wang, Qiannan Huang, Jun Zhu, Cheng Meng

Abstract

Many learning tasks represent responses as multivariate probability measures, requiring repeated computation of weighted barycenters in Wasserstein space. In multivariate settings, transport barycenters are often computationally demanding and, more importantly, are generally not well posed under the affine weight schemes inherent to global and local Fréchet regression, where weights sum to one but may be negative. We propose HiMAP, a Hilbert mass-aligned parameterization that endows multivariate measures with a distribution-invariant notion of quantile level. The construction recursively refines the domain through equiprobable conditional-median splits and follows a Hilbert curve ordering, so that a single scalar index consistently tracks cumulative probability mass across distributions. This yields an embedding into a Hilbert function space and induces a tractable discrepancy for distribution comparison and averaging. Crucially, the representation is closed under affine averaging, leading to a closed-form, well-posed barycenter and an explicit distribution-valued Fréchet regression estimator obtained by averaging HiMAP quantile maps. We establish consistency and a dimension-dependent polynomial convergence rate for HiMAP estimators under mild conditions, matching the classical rates for empirical convergence in multivariate Wasserstein geometry. Numerical experiments and a multivariate climate-indicator study demonstrate that HiMAP delivers barycenters and regression fits comparable to standard optimal-transport surrogates while achieving substantial speedups in schemes dominated by repeated barycenter evaluations.

Index Terms

Multivariate quantile, Distributional barycenter, Fréchet regression, Hilbert curve, Optimal transport

I. INTRODUCTION

In many modern statistical and machine learning pipelines, the response is naturally represented as a probability distribution rather than a finite-dimensional vector, and inference proceeds by comparing distributions and aggregating them into representative “central” objects [1], [2]. Among various distributional discrepancies, the Wasserstein distance is particularly attractive for its geometric interpretation and its sensitivity to support misalignment [3], [4]. Within this geometry, Wasserstein barycenters provide a canonical notion of an average distribution [5] and constitute a key computational primitive in downstream procedures. A prominent example is Fréchet regression with distribution-valued responses, where fitting requires repeated evaluation of *weighted* barycenters along the covariate domain [6]. Such barycenter-based learning tasks arise across applications, including OT-driven integration and harmonization of multisource single-cell datasets [7], Wasserstein-geometry-based representation and inference for complex objects (e.g., brain networks and imaging-derived features) [8], [9], and fairness/robust learning formulations that compute central distributions under Wasserstein constraints [10].

This paper addresses the challenge of constructing a multivariate analogue of the univariate quantile representation. Specifically, we seek a representation that yields a tractable and interpretable barycentric calculus at a shared ‘quantile level’. In one dimension, the W_2 geometry admits an isometric quantile-function representation, under which barycenters and related operators reduce to simple algebra performed pointwise in the common quantile index $t \in [0, 1]$ [4], [11]. This shared mass scale leads to explicit barycentric formulas and enables transparent statistical analysis. By contrast, in dimensions $d \geq 2$, multivariate distributions have long lacked an equally operational quantile-type representation that simultaneously (i) assigns a distribution-invariant meaning to the index t and (ii) is closed under the linear operations needed for barycentric aggregation.

The absence of such a representation becomes especially consequential in Fréchet regression. Canonical global and local Fréchet regression estimators are built from *affine* weights, i.e., weights that sum to one but may be negative [6]. Affine (signed) weights represent neither a theoretical anomaly nor a boundary condition; rather, they are intrinsic to local linear smoothing and also arise in global linear constructions. However, the standard multivariate Wasserstein barycenter problem is structurally aligned with *nonnegative* convex weights; under affine weights, the objective loses convexity, and the barycenter operation is generally ill-posed in the original Wasserstein space [5]. As a result, for multivariate distributional regression, one often necessitates reliance on either sophisticated geometric surrogates or iterative numerical solvers, and it becomes difficult to obtain both a tractable methodological formulation and a streamlined theoretical framework comparable to the univariate quantile case.

Existing approaches to scalable Wasserstein barycenters can be broadly categorized into three streams. The first category focuses on computational tractability of OT variational problems via entropic regularization (Sinkhorn) and its accelerations,

T. Wang, J. Zhu and C. Meng are affiliated with the Institute of Statistics and Big Data, Renmin University of China, Beijing, China. Q. Huang is affiliated with the Area of Innovation and Information Management, Faculty of Business and Economics, The University of Hong Kong, Hong Kong. Correspondence: C. Meng. Email: chengmeng@ruc.edu.cn.

as well as stochastic and approximate OT solvers [12]–[18]. Related work develops scalable barycenter routines for clustering, sequential, and distributed settings [19]–[21]. While powerful, these approaches still compute barycenters through iterative OT-type subroutines and do not directly address the structural difficulty posed by affine weights in multivariate settings. Alternatively, strictly geometric surrogates replace W_2 by more tractable surrogate geometries, notably sliced/projection-based Wasserstein variants [22]–[30]. These constructions accelerate comparison and matching by reducing multivariate structure to one-dimensional problems, yet they typically do not yield a distribution-invariant mass coordinate that supports closed-form barycentric operations under affine weights. A distinct line of research employs linearization techniques, for example via tangent-space representations in Wasserstein geometry [2] or related regression schemes based on transport-map parameterizations [31]. Such representations enable regression-style operations, but they usually require estimating high-dimensional OT maps relative to a reference distribution and therefore do not provide a broadly scalable, closed-form barycenter operator for general affine weights.

Our goal is to address this methodological gap: a multivariate representation that endows different distributions with a common mass scale (a shared “quantile level”) and is *closed under affine linear combinations*, so that weighted barycenters, including those arising in Fréchet regression, become explicit and well defined. To this end, we introduce the *Hilbert mass-aligned parameterization* (HiMAP), a probability-driven space-filling-curve construction that replaces purely geometric bisections by equiprobable recursive splits governed by conditional medians. The resulting parameterization enforces that the curve index advances synchronously with cumulative probability mass, thereby assigning a distribution-invariant meaning to $t \in [0, 1]$. This mass alignment induces an L^2 -type representation and a corresponding metric under which barycentric aggregation reduces to linear algebra at common t levels, restoring an analytic barycenter calculus analogous to the univariate quantile setting while remaining computationally lightweight.

Contributions: Our main contributions are fourfold.

- 1) We introduce HiMAP, a Hilbert mass-aligned parameterization for multivariate probability measures that embeds the curved Wasserstein geometry into a flat L^2 representation. The induced parametrization provides a distribution-invariant *quantile level* semantics and leads to analytic expressions for barycenters and distribution-valued Fréchet regression.
- 2) We develop a rigorous theoretical foundation for HiMAP, establishing the validity of the proposed HiMAP quantile map and its closure under affine combinations. We further prove the existence and uniqueness of the HiMAP barycenter under affine weights, and derive closed-form expressions for the barycenter and the corresponding Fréchet regression estimators.
- 3) We provide statistical guarantees for the resulting procedures. Specifically, we prove consistency of the empirical HiMAP quantile map, the induced barycenter, and the associated Fréchet regression estimator, and we derive ambient-dimension-dependent convergence rates under mild conditions; these rates are comparable to the classical polynomial rates characteristic of Wasserstein geometry [32].
- 4) We demonstrate, through simulations and real-data analyses, that HiMAP produces barycenters and regression fits that are comparable in regression estimation error and qualitative geometry to widely used optimal-transport surrogates in our benchmarks (Sections V–VI), while reducing runtime by near $100\times$ in repeated-barycenter regimes under same settings (Table IV).

Organization: Section II reviews Wasserstein geometry, barycenters, and Fréchet regression in metric space. Section III develops the HiMAP quantile function and its statistical properties. Section IV introduces the HiMAP barycenter and its Fréchet regression instantiation. Sections V and VI report simulations and a real-data study, followed by concluding remarks in Section VII.

II. PRELIMINARY

A. Notation

Scalars are denoted by lowercase letters (e.g., t, λ), vectors by bold lowercase letters (e.g., \mathbf{x}, \mathbf{u}), and matrices by bold uppercase letters; for $n \geq 1$, $[n] = \{1, \dots, n\}$. For $\mathbf{x} \in \mathbb{R}^d$, $\|\mathbf{x}\|$ and $\langle \mathbf{x}, \mathbf{y} \rangle$ denote the Euclidean norm and inner product; for $r \geq 1$ and measurable $f : [0, 1] \rightarrow \mathbb{R}^d$, $\|f\|_{L^r} = (\int_0^1 \|f(t)\|^r dt)^{1/r}$, and $\langle f, g \rangle_{L^2} = \int_0^1 \langle f(t), g(t) \rangle dt$. The indicator is $\mathbf{1}\{\cdot\}$ and \log is the natural logarithm. Let $\mathcal{P}(\mathbb{R}^d)$ be the set of Borel probability measures on \mathbb{R}^d , $\mathcal{P}_r(\mathbb{R}^d)$ those with finite r th moment, and $\mathcal{P}_\infty(\mathbb{R}^d)$ those supported on a bounded subset of \mathbb{R}^d ; for $\mu \in \mathcal{P}(\mathbb{R}^d)$, $\text{supp}(\mu)$ is its support and $\delta_{\mathbf{x}}$ is the Dirac measure at \mathbf{x} . Given i.i.d. $\mathbf{U}_1, \dots, \mathbf{U}_n \sim \mu$, the empirical measure is $\hat{\mu}_n = n^{-1} \sum_{j=1}^n \delta_{\mathbf{U}_j}$; for a measurable map T , $T_{\#}\mu$ denotes the pushforward, and for μ, ν we write $\Pi(\mu, \nu)$ for the set of couplings. In regression settings we observe i.i.d. pairs $\{(\mathbf{X}_i, Y_i)\}_{i=1}^m$ with predictors $\mathbf{X}_i \in \mathbb{R}^p$ and distribution-valued responses $Y_i \in \mathcal{P}_\infty(\mathbb{R}^d)$; when needed, $\{\mathbf{U}_{ij}\}_{j=1}^n \sim Y_i$ denotes an internal sample from Y_i . We use $a_n \lesssim b_n$ for $a_n \leq Cb_n$ with a universal constant $C > 0$, $a_n \asymp b_n$ when both directions hold, and the usual stochastic orders $O_p(\cdot)$, $o_p(\cdot)$, with \rightarrow_p denoting convergence in probability; generic constants $c, C > 0$ may change from line to line.

B. Wasserstein geometry and the one-dimensional reference structure

1) *Wasserstein distance and the quantile representation in one dimension:* Optimal transport (OT) provides a principled geometric framework for comparing probability measures. Let $r \geq 1$, and $\mathcal{P}_r(\mathbb{R}^d)$ denote the space of Borel probability measures on \mathbb{R}^d with finite r -th moments. The r -Wasserstein distance between $\mu, \nu \in \mathcal{P}_r(\mathbb{R}^d)$ is defined as

$$W_r(\mu, \nu) = \left(\inf_{\gamma \in \Pi(\mu, \nu)} \int_{\mathbb{R}^d \times \mathbb{R}^d} \|\mathbf{x} - \mathbf{y}\|^r d\gamma(\mathbf{x}, \mathbf{y}) \right)^{1/r},$$

where $\Pi(\mu, \nu)$ denotes the set of couplings with marginals μ and ν [3]. In the one-dimensional case ($d = 1$), the Wasserstein space exhibits a special geometry isometric to a convex subset of $L^2([0, 1])$. Specifically, let F_μ^{-1} be the quantile function of μ . Then, W_2 admits the explicit representation [4], [11]:

$$W_2^2(\mu, \nu) = \int_0^1 |F_\mu^{-1}(t) - F_\nu^{-1}(t)|^2 dt. \quad (1)$$

This formula allows distributions to be compared pointwise at a common probability level $t \in [0, 1]$.

2) *Wasserstein barycenters and linear closure at the quantile level:* Given measures $\nu_1, \dots, \nu_q \in \mathcal{P}_2(\mathbb{R}^d)$ and weights $\lambda_1, \dots, \lambda_q$ summing to one, the Wasserstein barycenter is defined as the minimizer of the Fréchet functional [5]:

$$\nu^* = \arg \min_{\nu \in \mathcal{P}_2(\mathbb{R}^d)} \sum_{j=1}^q \lambda_j W_2^2(\nu_j, \nu).$$

When $d = 1$, substituting (1) into the objective reduces the problem to a pointwise weighted least-squares minimization in the quantile space. Consequently, the barycenter admits a closed-form characterization:

$$F_{\nu^*}^{-1}(t) = \sum_{j=1}^q \lambda_j F_{\nu_j}^{-1}(t), \quad t \in [0, 1].$$

Thus, for $d = 1$, computing the barycenter is equivalent to taking a weighted linear combination of quantile functions. Crucially, the set of univariate quantile functions is a convex cone, ensuring that convex combinations remain valid quantile functions.

3) *Comparison of multivariate barycenter methodologies:* In dimensions $d \geq 2$, the convenient univariate quantile representation generally ceases to exist, and the Wasserstein space loses its flat geometry. Consequently, computing a barycenter requires solving a variational problem dependent on the specific discrepancy metric. To assess their suitability for tasks such as Fréchet regression, where weights are typically *affine* and may be signed, we categorize representative approaches based on four attributes: the existence of an *explicit expression*, the capacity to handle *affine weights*, the reliance on *iterative OT solvers*, and *computational complexity*. The computational model considered in this paper is a free-support barycenter problem with the same number of support points as the input.

- 1) *Exact Wasserstein Barycenter (WB):* Defined via the standard W_2 distance, the exact barycenter requires solving a large-scale linear programming or variational problem with complexity $\mathcal{O}(Tqn^3 \log n)$. Crucially, the W_2 objective is convex only for non-negative weights; under affine weights, the problem becomes non-convex and generally ill-posed.
- 2) *Sinkhorn Wasserstein Barycenter:* Entropic regularization accelerates computation via matrix scaling algorithms (e.g., Sinkhorn-Knopp) to $\mathcal{O}(n^2)$ [12]. However, the method remains iterative and relies on the positivity of transport plans, failing to support affine combinations naturally.
- 3) *Sliced Wasserstein Barycenter (SWB):* SWB projects distributions onto one-dimensional lines where closed-form solutions exist [22]. While computationally efficient ($\mathcal{O}(n \log n)$ per slice), recovering the high-dimensional barycenter requires iterative optimization. Moreover, linear combinations of 1D quantiles with negative weights may violate monotonicity, yielding invalid inverse Radon transforms.

In contrast, the proposed *HIMAP Barycenter* leverages a Hilbert mass-aligned parameterization to embed distributions into an L^2 space. As summarized in Table I, our method satisfies all criteria. It operates in a vector space, naturally supporting *affine weights*, offering an *explicit expression*, and achieving a non-iterative complexity of $\mathcal{O}(qn \log n)$.

C. Distribution-valued Fréchet regression and weighted barycenters

Fréchet regression generalizes classical regression to metric-space-valued responses [6]. Let (\mathcal{F}, d) be a metric space. For a predictor $\mathbf{X} \in \mathbb{R}^p$ and a response $Y \in \mathcal{F}$, the conditional Fréchet mean is defined as

$$m_{\oplus}(\mathbf{x}) \in \arg \min_{\omega \in \mathcal{F}} \mathbb{E}[d^2(Y, \omega) \mid \mathbf{X} = \mathbf{x}].$$

Canonical estimators for $m_{\oplus}(\mathbf{x})$ employ global or local linear weights $w_i(\mathbf{x})$, constructed from the predictor samples $\{(\mathbf{X}_i)\}_{i=1}^n$:

- (1) *Global linear weights:*

$$w^{(G)}(\mathbf{z}, \mathbf{x}) = 1 + (\mathbf{z} - \boldsymbol{\mu})^\top \boldsymbol{\Sigma}^{-1}(\mathbf{x} - \boldsymbol{\mu}),$$

TABLE I

STRUCTURAL COMPARISON OF REPRESENTATIVE ROUTES TO BARYCENTERS. n DENOTES SAMPLE SIZE, q IS THE NUMBER OF DISTRIBUTIONS, AND T IS THE ITERATION COUNT.

Route	Closed-form	Affine wts.	Iterative OT	Complexity
WB	No	No	Yes	$\mathcal{O}(Tqn^3 \log n)$
Sinkhorn WB	No	No	Yes	$\mathcal{O}(Tqn^2)$
Sliced WB	No	No	Yes	$\mathcal{O}(Tqn \log n)$
HiMAP barycenter (this paper)	Yes	Yes	No	$\mathcal{O}(qn \log n)$

where $\boldsymbol{\mu}$ and $\boldsymbol{\Sigma}$ are the population mean and covariance of \mathbf{X} .

(2) *Local linear weights (scalar $p = 1$):*

$$w^{(L)}(z, x; h) = \frac{1}{\sigma_0^2(x; h)} K_h(z - x) \left[\mu_2(x; h) - \mu_1(x; h)(z - x) \right],$$

where $\mu_j(x; h) = \mathbb{E}_X \left[K_h(X - x)(X - x)^j \right]$ and $\sigma_0^2 = \mu_0\mu_2 - \mu_1^2$ using kernel notations from [6].

In the distribution-valued setting where $(\mathcal{F}, d) = (\mathcal{P}_2(\mathbb{R}^d), W_2)$, the estimator takes the form of a weighted Wasserstein barycenter:

$$\hat{m}(\mathbf{x}) \in \arg \min_{\omega \in \mathcal{P}_2(\mathbb{R}^d)} \sum_{i=1}^n w_i(\mathbf{x}) W_2^2(Y_i, \omega).$$

Denote $w^{(G)}(\mathbf{X}_i, \mathbf{x})$ or $w^{(L)}(\mathbf{X}_i, \mathbf{x}, h)$ as $w_i(\mathbf{x})$. A critical feature of these weights is that they are *affine*, meaning $\sum w_i(\mathbf{x}) = 1$ but individual $w_i(\mathbf{x})$ can be negative. In the one-dimensional case ($d = 1$), the estimator admits a strictly closed-form solution via the quantile representation: $\hat{F}_{m(\mathbf{x})}^{-1}(t) = \sum_{i=1}^n w_i(\mathbf{x}) F_{Y_i}^{-1}(t)$. However, for multivariate distributions ($d \geq 2$), this linear structure is lost. Since the standard Wasserstein space is not a vector space, affine combinations with negative weights are generally ill-posed. Existing approaches, such as conditional Wasserstein barycenters [31], typically address this by regressing optimal transport maps in a tangent space relative to a reference distribution. This limitation motivates the search for a multivariate parameterization that recovers a vector-space structure analogous to the univariate quantile, thereby enabling direct linear aggregation with affine weights.

III. A HILBERT MASS-ALIGNED PARAMETERIZATION QUANTILE FUNCTION FOR MULTIVARIATE DISTRIBUTIONS

This section develops the Hilbert mass-aligned parameterization (HiMAP), a framework designed to bridge the structural gap between univariate and multivariate quantile representations. Our primary goal is to construct a transport-type function that aligns the geometry of the support with the accumulated probability mass, thereby enabling linear operations in the Wasserstein space. Section III-A introduces the probability-driven recursive partition that constructs the population-level Hilbert Mass-aligned Parameterization $\mathbf{H}_{\mu, L}$. Section III-B defines the limiting HiMAP quantile function \mathbf{Q}_μ and characterizes its geometric properties. Section III-C details the computational implementation via a tree structure. Finally, Section III-D derives the statistical convergence rates of the empirical estimator.

Throughout, we assume $\mu \in \mathcal{P}_\infty(\mathbb{R}^d)$ with support \mathcal{S} contained in a bounded axis-aligned box $\mathcal{M} = \prod_{j=1}^d [L_{0,j}, U_{0,j}]$. We denote a support vector by $\mathbf{u} \in \mathbb{R}^d$.

A. Construction of Fine-depth Hilbert Mass-aligned parameterization

Hilbert space-filling curves: Space-filling curves, such as the Peano and Hilbert curves, are continuous surjections from the unit interval onto a hypercube [33]. These curves induce a deterministic linear ordering of the high-dimensional space, preserving locality at finite resolutions. While our framework admits general recursive space-filling schemes, we adopt the Hilbert curve for its superior distance-preserving properties. Fig. 1 visualizes the first three orders of the Hilbert curve. As the order increases, this curve becomes space-filling, visiting every point in the domain in the limit.

Construction procedure via mass-aligned partitions: Standard space-filling curve constructions partition space based on geometric features (e.g., midpoint of axis). While sufficient for uniform distributions, geometric partitioning fails to capture the mass concentration of arbitrary measures. To address this, we propose a *mass-aligned* recursion.

Let $s : \mathbb{N} \rightarrow \{1, \dots, d\}$ be a coordinate splitting schedule. A balanced choice is the cyclic schedule $s(l) = 1 + ((l - 1) \bmod d)$. Let $\mathcal{B}_0 = \mathcal{M} \cap \mathcal{S}$. At step l , we partition \mathcal{B}_0 into 2^l subcells that are equiprobable but generally of unequal geometric size. For $l \geq 1$, consider a parent cell $\mathcal{B}_{l-1} = \prod_{j=1}^d [L_{l-1,j}, U_{l-1,j}] \cap \mathcal{S}$ generated at the previous step. We define the *conditional median cut* along coordinate $j_l = s(l)$ as:

$$q_l(\mu; \mathcal{B}_{l-1}) := \inf \left\{ x \in \mathbb{R} : \mu(\{\mathbf{u} \in \mathcal{B}_{l-1} : u_{j_l} \leq x\}) \geq \frac{1}{2} \mu(\mathcal{B}_{l-1}) \right\}. \quad (2)$$

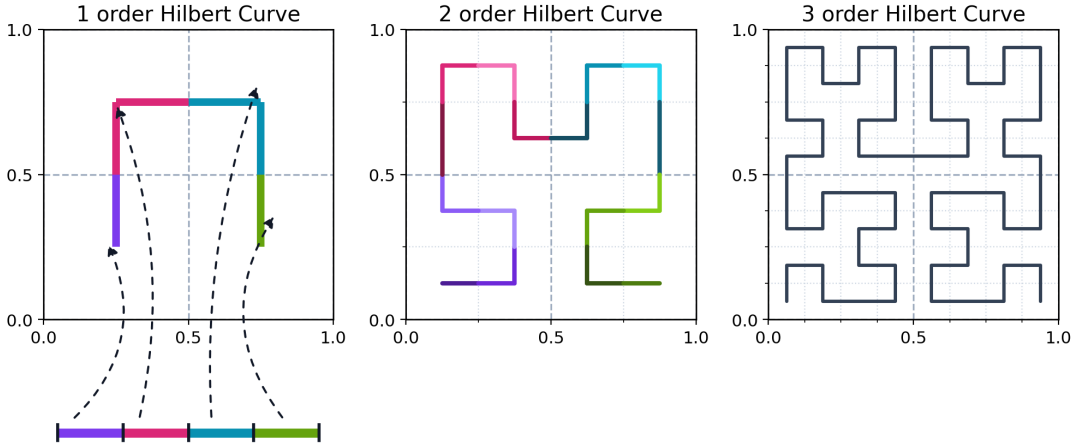


Fig. 1. Illustration of the first three orders of the Hilbert curve construction.

This cut partitions \mathcal{B}_{l-1} into two children cells, $\mathcal{B}_{l-1}^{(0)}$ (lower half) and $\mathcal{B}_{l-1}^{(1)}$ (upper half), by replacing the j_l -th interval with $[L_{l-1,j_l}, q_l]$ and $[q_l, U_{l-1,j_l}]$, respectively. By construction, this ensures an equiprobable split:

$$\mu\left(\mathcal{B}_{l-1}^{(0)}\right) = \mu\left(\mathcal{B}_{l-1}^{(1)}\right) = \frac{1}{2}\mu\left(\mathcal{B}_{l-1}\right). \quad (3)$$

For any $t \in [0, 1]$, the Hilbert curve induces a unique mapping to a sequence of nested sub-cells. Specifically, the parameter t encodes a path through the hierarchy of cells, denoted as $\{\mathcal{B}_l(t)\}_{l \geq 0}$, such that $\mathcal{B}_l(t)$ is the specific depth- l cell containing the image of t under the Hilbert mapping. The precise correspondence between the expansion of t (e.g., in base-4 for $d = 2$) and the cell indices is determined by the orientation-preserving rules of the Hilbert curve; we defer the detailed combinatorial definition to Appendix A.

Notably, since each split halves the probability mass, the cell $\mathcal{B}_l(t)$ represents a localized region of measure 2^{-l} . The finite-depth map $\mathbf{H}_{\mu,L}(t)$ is defined as a representative point within the terminal cell $\mathcal{B}_L(t)$. A convenient choice is the vector of the most recent cut points along each dimension. Let $k_j(L)$ be the largest depth $l \leq L$ such that $s(l) = j$. We define:

$$\mathbf{H}_{\mu,L}(t) := \left(q_{k_1(L)}(t), q_{k_2(L)}(t), \dots, q_{k_d(L)}(t)\right)^\top, \quad (4)$$

where $q_l(t)$ abbreviates $q_l(\mu; \mathcal{B}_{l-1}(t))$.

Remark 1. The map $\mathbf{H}_{\mu,L}$ differs fundamentally from purely geometry-driven space-filling curves. As illustrated in Fig. 2, geometric constructions (panel (a)) rely on fixed spatial boundaries, whereas our approach (panel (b)) is probability-driven, allocating higher resolution to high-density regions. The path index t advances synchronously with the cumulative probability mass of μ , creating a distribution-invariant coordinate system essential for Wasserstein geometry.

Remark 2 (Local Logical Coordinates and Reflections). Note that the splitting schedule $s(l)$ operates on the local logical coordinates of each sub-cell. Due to the orientation-preserving reflections inherent to the Hilbert curve (which swap axes in certain sub-quadrants, such as the lower-left and lower-right sub-quadrants after the first two rounds of splitting in Fig. 2 (b), to maintain spatial continuity), a logical x -split at depth l may correspond to a geometric y -split in the global coordinate system for specific branches. This local coordinate adaptation ensures the continuity of the curve while maintaining the balanced refinement of all geometric dimensions required for our theoretical guarantees. A detailed illustration of the Hilbert ordering rule is provided in Appendix A.

B. Properties of the Hilbert Mass-aligned Parameterization Quantile Function

We now formally define the HiMAP quantile function as the limit of the finite-depth maps. To ensure well-posedness, we impose the following regularity conditions.

Assumption 3. A.1 The measure $\mu \in \mathcal{P}_\infty(\mathbb{R}^d)$ admits a density f supported on \mathcal{M} satisfying $0 < m \leq f(\mathbf{u}) \leq M < \infty$ for all $\mathbf{u} \in \mathcal{M}$.

A.2 For each depth l , the conditional median in (2) is unique.

A.3 The splitting schedule $s(l)$ is balanced: there exists a constant $c_s > 0$ such that for any coordinate j and depth L , the number of splits along j satisfies $\#\{l \leq L : s(l) = j\} \geq c_s L/d$.

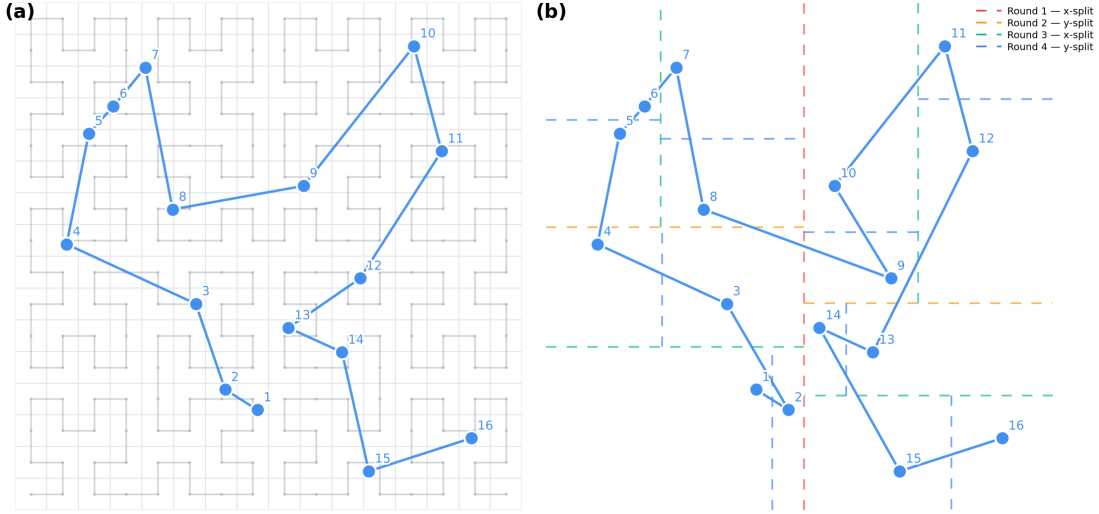


Fig. 2. Comparison of construction policies. (a) Geometry-driven approach: partitions space based on a fixed spatial metric, sensitive to support boundaries. (b) Mass-aligned approach (Ours): recursively splits cells by conditional medians, adapting to the underlying density. The legend in (b) denotes splits along the *logical* axes; note that in the lower-left and lower-right quadrants, the Round 3 logical x -split maps to a horizontal geometric split due to Hilbert coordinate reflections.

Assumption 3 (A.1)–(A.2) guarantees that each conditional median cut is well-defined and stable, so the recursion produces a unique nested cell sequence and an identifiable limit map. Assumption 3 (A.3) ensures that every dimension is refined indefinitely. Combined with the density bounds in (A.1), this forces the geometry of the cells to contract. For the Hilbert space-filling curve $c_s = 1$.

Lemma 4 (Geometric Decay of Cell Diameters). *Under Assumption 3, the diameter of the path cells shrinks exponentially. Specifically, let $\rho = 1 - \frac{m}{2M} \in (0, 1)$, there exists $C > 0$ such that for all L and t ,*

$$\text{diam}(\mathcal{B}_L(t)) \leq C\rho^{c_s L/d},$$

This geometric decay implies that for any fixed t , the sequence $\{\mathbf{H}_{\mu,L}(t)\}_{L \geq 1}$ is Cauchy. This justifies the existence of the limiting map.

Lemma 5 (Existence of Limiting Map). *Under Assumption 3, there exists a measurable map $\mathbf{H}_\mu : [0, 1] \rightarrow \mathbb{R}^d$ such that for all $t \in [0, 1]$ with a unique expansion representation,*

$$\mathbf{H}_\mu(t) = \lim_{L \rightarrow \infty} \mathbf{H}_{\mu,L}(t).$$

Based on this limit, we define our multivariate quantile function.

Definition 6. *The Hilbert Mass-aligned parameterization (HiMAP) quantile function of μ is defined as:*

$$\mathbf{Q}_\mu(t) := \lim_{L \rightarrow \infty} \mathbf{H}_{\mu,L}(t), \quad t \in [0, 1]. \quad (5)$$

The HiMAP quantile \mathbf{Q}_μ serves as a canonical transport map from the uniform distribution to μ , establishing a unified “quantile level” across multivariate distributions.

Theorem 7 (Pushforward Identification). *Under Assumption 3, the map pushes the uniform measure to the target distribution: $(\mathbf{Q}_\mu)_\# \text{Unif}[0, 1] = \mu$. Consequently, the mapping $\mu \mapsto \mathbf{Q}_\mu$ is identifiable up to a null set in t .*

Theorem 7 implies that \mathbf{Q}_μ induces a distribution-invariant mass index in $\mathcal{P}_\infty(\mathbb{R}^d)$. Consequently, distribution comparison can be carried out by the L^r distance between the corresponding \mathbf{Q} -maps.

Proposition 8. *Under Assumption 3, \mathbf{Q}_μ satisfies:*

- (i) **Coordinate-wise Affine Equivariance:** *If $T(\mathbf{u}) = \mathbf{A}\mathbf{u} + \mathbf{b}$ with diagonal $\mathbf{A} \succ 0$, then $\mathbf{Q}_{T\#\mu}(t) = \mathbf{A}\mathbf{Q}_\mu(t) + \mathbf{b}$ for a.e. t .*
- (ii) **L^r Embedding:** *The map $\Phi : \mu \mapsto \mathbf{Q}_\mu$ embedding $(\mathcal{P}_\infty(\mathbb{R}^d))$ into $L^r([0, 1]; \mathbb{R}^d)$, induces a well-defined metric*

$$d_{\text{HiMAP},r}^r(\mu, \nu) = \int_0^1 \|\mathbf{Q}_\mu(t) - \mathbf{Q}_\nu(t)\|^r dt.$$

And, $d_{\text{HiMAP},r}$ is a stronger topology compared to Wasserstein distance, i.e.,

$$W_r(\mu, \nu) \leq d_{\text{HiMAP},r}(\mu, \nu).$$

(iii) **Linear Closure:** For any $\{\mu_i\}_{i=1}^q$ and weights satisfying $\sum \lambda_i = 1$ (including affine weights), the linear combination $\sum_{i=1}^q \lambda_i \mathbf{Q}_{\mu_i}$ corresponds to the HiMAP quantile function of a valid probability measure.

Proposition 8 (iii) is the most critical feature for barycenter and Fréchet regression. Under the standard Wasserstein geometry, barycenters with affine (i.e., possibly negative) weights are not well defined. However, the set of HiMAP quantile functions is closed under affine combinations. This closure property guarantees that when we compute weighted averages (even with negative weights), the result remains a valid, interpretable probability distribution.

C. Algorithmic Implementation

Having defined the population-level map, we now address its practical computation given a finite sample $\mathbf{U}_1, \dots, \mathbf{U}_n \sim \mu$. The construction is realized via a binary tree where each node represents a sub-cell and stores the associated sample indices and splitting threshold.

Algorithm 1 outlines the recursive construction. At each step, we identify the active sample subset \mathcal{I} , compute the empirical median along the scheduled coordinate $j = s(\ell)$, and partition the indices into two children.

Algorithm 1 Hilbert Mass-aligned Parameterization Tree Construction (Depth L)

Require: Samples $\{\mathbf{U}_i\}_{i=1}^n$, depth L , schedule $s(1:L)$. $s(l)$ is the local logical coordinate for different l -depth sub-cell.

- 1: Initialize root node with index set $\mathcal{I}_0 = \{1, \dots, n\}$
 - 2: **for** $\ell = 1$ to L **do**
 - 3: **for** each node at depth $\ell - 1$ with index set \mathcal{I} **do**
 - 4: Set coordinate $j \leftarrow s(\ell)$.
 - 5: Compute empirical median \hat{q} of $\{(\mathbf{U}_i)_j : i \in \mathcal{I}\}$
 - 6: Partition \mathcal{I} into $\mathcal{I}^{(0)} = \{i \in \mathcal{I} : (\mathbf{U}_i)_j \leq \hat{q}\}$ and $\mathcal{I}^{(1)} = \mathcal{I} \setminus \mathcal{I}^{(0)}$
 - 7: Store split parameters (j, \hat{q}) and create child nodes with $\mathcal{I}^{(0)}, \mathcal{I}^{(1)}$
 - 8: if $\#\mathcal{I}^{(0)} = 0$ or $\#\mathcal{I}^{(1)} = 0$, this node stop splitting.
 - 9: **end for**
 - 10: **end for**
 - 11: **return** Depth- L tree with split values
-

Once the tree is built, evaluating the empirical quantile $\hat{\mathbf{Q}}_{\mu,L}(t)$ reduces to a tree traversal. The parameter t determines the path (via the rules in Appendix A), and the estimator retrieves the sequence of stored cuts.

Algorithm 2 Evaluation of Empirical Quantile $\hat{\mathbf{Q}}_{\mu,L}(t)$

Require: Depth- L tree, $t \in [0, 1]$, schedule $s(1:L)$

- 1: Determine path indices (bits) based on t and Hilbert ordering rules
 - 2: Traverse tree from root to leaf following the path
 - 3: Collect the most recent cut value for each coordinate $j \in \{1, \dots, d\}$
 - 4: **return** $\hat{\mathbf{Q}}_{\mu,L}(t) \in \mathbb{R}^d$
-

The computational complexity is governed by the median finding and partitioning. Using linear-time selection (e.g., Quick-select), building the tree requires $\mathcal{O}(nL)$ time. Querying a single t takes $\mathcal{O}(L)$. Thus, evaluating the quantile function on a grid of size m costs $\mathcal{O}(nL + mL)$. Since L typically scales logarithmically with n , this method is highly efficient compared to iterative optimal transport solvers.

D. Sample Estimation and Convergence

We now analyze the statistical properties of the estimator produced by Algorithm 1. The sample construction $\hat{\mathbf{Q}}_{\mu,L}(t)$ can be viewed as the solution to a recursive Z-estimation problem.

At depth l , given the empirical cell $\hat{\mathcal{B}}_{l-1}(t)$, the splitting value is the root of the empirical estimating equation:

$$\hat{\Psi}_l(q; t) := \frac{1}{n} \sum_{i=1}^n \left(\mathbf{1} \left\{ \mathbf{U}_i \in \hat{\mathcal{B}}_{l-1}(t), (\mathbf{U}_i)_{j_l} \leq q \right\} - \frac{1}{2} \mathbf{1} \left\{ \mathbf{U}_i \in \hat{\mathcal{B}}_{l-1}(t) \right\} \right).$$

Let $\hat{q}_l(t)$ denote the solution (empirical conditional median). By inductively propagating estimation errors through the levels of the tree, we establish the pointwise consistency and convergence rate of the resulting map.

Theorem 9 (Pointwise Convergence). *Let $\mu \in \mathcal{P}_\infty(\mathbb{R}^d)$, $s(l)$ and constant c_s satisfy Assumption 3. Given $t \in [0, 1]$ associated with the nested sub-cell sequence $\{\mathcal{B}_l(t)\}_{l=1}^L$ based on Hilbert curve ordering rules. Consider the estimator $\hat{\mathbf{Q}}_{\mu,L}(t)$ constructed*

with depth $L \asymp \log n$. Then, there exists a constant $\gamma > 0$ depending on the density bounds and support geometry (explicit constants defined in Appendix C-E), as $n \rightarrow \infty$,

$$\left\| \widehat{\mathbf{Q}}_{\mu,L}(t) - \mathbf{Q}_{\mu}(t) \right\|_2 = O_p \left(n^{-\frac{c_s}{2d\gamma}} \right),$$

Theorem 9 highlights that while the method is computationally efficient, the statistical rate depends on the dimension d , reflecting the curse of dimensionality inherent in multivariate non-parametric estimation. Since the error bounds hold uniformly in t , we obtain a corresponding rate for the HiMAP distance.

Corollary 10 (L^2 Convergence). *Under the conditions of Theorem 9, the sample estimator is consistent in the 2-HiMAP metric:*

$$d_{\text{HiMAP},2}(\widehat{\mu}_n, \mu) = \left(\int_0^1 \left\| \widehat{\mathbf{Q}}_{\mu,L}(t) - \mathbf{Q}_{\mu}(t) \right\|_2^2 dt \right)^{1/2} = O_p \left(n^{-\frac{c_s}{2d\gamma}} \right).$$

Corollary 10 establishes a statistical convergence guarantee for the L^2 metric induced by HiMAP, and shows that its convergence rate is comparable to that of the Wasserstein distance in d -dimension [32]; in particular, both rates are sensitive to the ambient dimension. This also reflects that they are highly sensitive to quantization error on the underlying support.

These results provide the theoretical justification for using HiMAP in barycenter computation and regression tasks, ensuring that empirical approximations converge to their population targets.

IV. HiMAP BARYCENTER AND FRÉCHET REGRESSION

Building on the theoretical foundation established in Section III, we now turn to the aggregation of multivariate distributions. The embedding Φ (Proposition 8) transforms the nonlinear Wasserstein geometry into a standard Hilbert space. This structural breakthrough allows us to solve the barycenter problem analytically and extend it to Fréchet regression with affine weights, a setting that remains computationally intractable or ill-posed under the classical Wasserstein framework.

A. Analytic Barycenters in HiMAP Geometry

Consider a collection of probability measures $\nu_1, \dots, \nu_q \in \mathcal{P}_{\infty}(\mathbb{R}^d)$. We seek a representative measure ν that minimizes a weighted sum of squared distances. Unlike the standard Wasserstein barycenter, which requires iterative optimization, the HiMAP geometry admits a closed-form solution.

Let $\lambda_1, \dots, \lambda_q \in \mathbb{R}$ be a set of weights. We explicitly allow for *affine weights* (where some $\lambda_i < 0$), provided that,

$$\Lambda := \sum_{i=1}^q \lambda_i > 0.$$

The HiMAP barycenter is defined as the minimizer of the Fréchet functional:

$$\nu_{\oplus} \in \operatorname{argmin}_{\nu \in \mathcal{P}_{\infty}(\mathbb{R}^d)} \mathcal{F}(\nu) := \sum_{i=1}^q \lambda_i d_{\text{HiMAP},2}^2(\nu_i, \nu). \quad (6)$$

Theorem 11 (Existence, Uniqueness, and Closed Form). *Under the metric d_{HiMAP} , the minimizer ν_{\oplus} exists and is unique. Furthermore, its corresponding HiMAP quantile function is given by the normalized affine combination:*

$$\mathbf{Q}_{\nu_{\oplus}}(t) = \frac{1}{\Lambda} \sum_{i=1}^q \lambda_i \mathbf{Q}_{\nu_i}(t), \quad t \in [0, 1]. \quad (7)$$

Consequently, the barycenter distribution is recovered as the pushforward $\nu_{\oplus} = (\mathbf{Q}_{\nu_{\oplus}})_{\#} \text{Unif}[0, 1]$.

The validity of this closed-form solution rests on the *Linear Closure* property (Proposition 8(iii)). Since the embedding space $L^2([0, 1]; \mathbb{R}^d)$ is a vector space, the affine combination on the RHS of (7) defines a valid function in the image of Φ , which uniquely corresponds to a probability measure in $\mathcal{P}_{\infty}(\mathbb{R}^d)$.

Remark 12 (Handling Affine Weights). *The ability to handle affine weights is a distinct advantage of the HiMAP framework over classical Wasserstein approaches. In standard optimal transport, barycenters are typically restricted to convex weights ($\lambda_i \geq 0$) because the Wasserstein space lacks negative curvature; minimizing a functional with negative weights is generally ill-posed or non-convex. However, in our framework, the embedding Φ linearizes the problem, ensuring that the global minimizer remains well-defined and unique even when weights are negative, as long as $\Lambda \geq 0$. This property is crucial for Fréchet regression methods, which inherently generate negative weights.*

Plug-in Estimation: The analytic structure implies that statistical estimation satisfies a "plug-in" principle. Suppose we observe samples from each distribution, $\mathbf{U}_{i,n_i} \sim \nu_i$. We first compute the individual estimators $\widehat{\mathbf{Q}}_{\nu_i, L_i}$ using Algorithm 1. The empirical barycenter is then simply:

$$\widehat{\mathbf{Q}}_{\nu_{\oplus}}(t) = \frac{1}{\Lambda} \sum_{i=1}^q \lambda_i \widehat{\mathbf{Q}}_{\nu_i, L_i}(t).$$

Fig. 3 illustrates the estimation procedure for the HiMAP barycenter. By the triangle inequality and the linearity of the

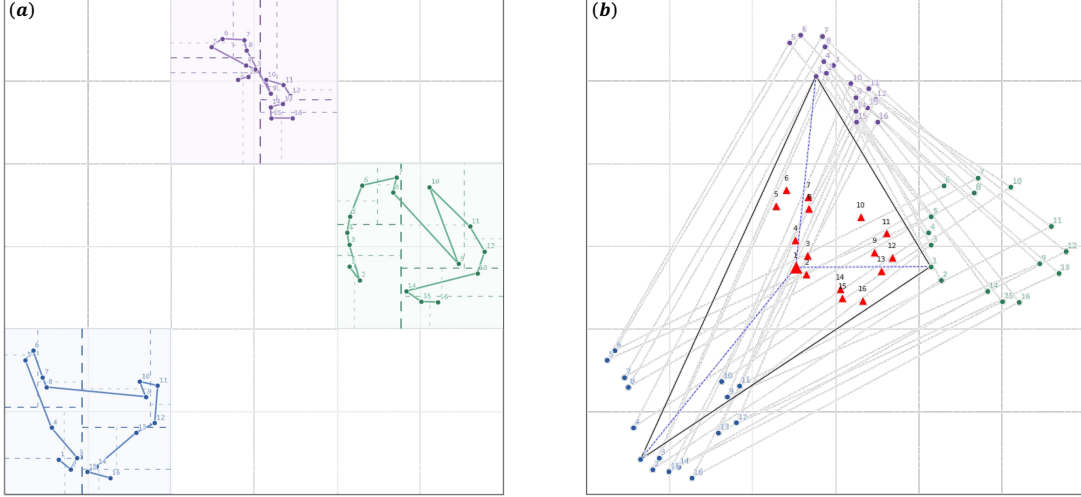


Fig. 3. Barycenter estimation procedure. For each sample U_{i,n_i} , we estimate the HiMAP quantile function via Algorithm 1 and 2. (b) Computing the barycenter is then equivalent to taking a weighted sum of these quantile functions, i.e., performing a weighted aggregation of the discrete support points at each shared quantile level. The resulting red point cloud represents the estimated HiMAP barycenter distribution.

combination, the estimation error of the barycenter is bounded by the weighted sum of the individual estimation errors derived in Corollary 10.

B. Fréchet Regression with Distributional Responses

We apply the barycentric framework to regression. Let (\mathbf{X}, Y) be a random pair where $\mathbf{X} \in \mathbb{R}^p$ is a predictor vector and $Y \in \mathcal{P}_{\infty}(\mathbb{R}^d)$ is a distribution-valued response. Following [6], the conditional Fréchet mean at a target point $\mathbf{x} \in \mathbb{R}^p$ is defined as:

$$m_{\oplus}(\mathbf{x}) = \operatorname{argmin}_{\omega \in \mathcal{P}_{\infty}(\mathbb{R}^d)} \mathbb{E} [w(\mathbf{X}, \mathbf{x}) d_{\text{HiMAP}, 2}^2(Y, \omega)],$$

where $w(\mathbf{X}, \mathbf{x})$ is a weight function satisfying $\mathbb{E}[w(\mathbf{X}, \mathbf{x})] = 1$. Applying Theorem 11, the population regression target is explicitly identified by the conditional expectation of the quantile functions:

$$\mathbf{Q}_{m_{\oplus}(\mathbf{x})}(t) = \mathbb{E} [w(\mathbf{X}, \mathbf{x}) \mathbf{Q}_Y(t)]. \quad (8)$$

This formulation generalizes classical Euclidean regression to the space of distributions: the regression target is simply the weighted average of the response maps \mathbf{Q}_Y .

Sample Estimators: Consider an observed dataset $\{(\mathbf{X}_i, Y_i)\}_{i=1}^m$, where for each Y_i , we observe independent samples $\mathbf{U}_{i,1}, \dots, \mathbf{U}_{i,n} \sim Y_i$. Let $\widehat{w}_i(\mathbf{x})$ be the empirical weights derived from the predictors $\{\mathbf{X}_i\}_{i=1}^m$. We define the Fréchet regression estimator $\widehat{m}(\mathbf{x})$ via its quantile function:

$$\widehat{\mathbf{Q}}_{m(\mathbf{x})}(t) = \sum_{i=1}^n \widehat{w}_i(\mathbf{x}) \widehat{\mathbf{Q}}_{Y_i}(t), \quad t \in [0, 1],$$

where $\widehat{\mathbf{Q}}_{Y_i}$ is the tree-based estimator for the i -th response. This estimator covers two canonical regression schemes:

- *Global Fréchet Regression:* Using the global linear weights $w^{(G)}(\mathbf{x})$ [6], we obtain the estimator $\widehat{m}^{(G)}(\mathbf{x})$.
- *Local Fréchet Regression:* Using kernel-based local linear weights $w^{(L)}(\mathbf{x}; h)$ with bandwidth h , we obtain the estimator $\widehat{m}^{(L)}(\mathbf{x})$.

Convergence Analysis: The consistency of these estimators follows from the convergence of the individual HiMAP quantiles (Theorem 9) and the consistency of the weights. Following the argument of [6], we obtain the following error decomposition. The detailed assumptions and proofs are provided in the Appendix D-B for completeness.

Corollary 13 (Regression consistency under $d_{\text{HiMAP},2}$ (global and local)). *Suppose the responses Y_i , constant c_s and splitting schedule $s(l)$ satisfy the regularity conditions of Assumption 3 and constant γ satisfies Thm 9, so that Corollary 10 holds. Let $\hat{m}^{(G)}(\mathbf{x})$ and $\hat{m}^{(L)}(\mathbf{x})$ be defined by*

$$\hat{\mathbf{Q}}_{m(\mathbf{x})}(t) = \sum_{i=1}^m \hat{w}_i(\mathbf{x}) \hat{\mathbf{Q}}_{Y_i}(t), \quad t \in [0, 1],$$

with $\hat{w}_i(\mathbf{x}) = \hat{w}_i^{(G)}(\mathbf{x})$ or $\hat{w}_i(\mathbf{x}) = \hat{w}_i^{(L)}(\mathbf{x}; h)$. Assume Assumption 17 for the global case and Assumption 18 for the local case hold (detailed in Appendix D-B). Then as $m \rightarrow \infty$ and $n \rightarrow \infty$, and for the local case $h \rightarrow 0$ with $mh^p \rightarrow \infty$,

$$d_{\text{HiMAP},2}(\hat{m}^{(G)}(\mathbf{x}), m_{\oplus}(\mathbf{x})) = O_p\left(\sqrt{\frac{p}{m}} + n^{-\frac{c_s}{2d\gamma}}\right),$$

$$d_{\text{HiMAP},2}(\hat{m}^{(L)}(\mathbf{x}), m_{\oplus}(\mathbf{x})) = O_p\left(h^2 + \frac{p}{\sqrt{mh^p}} + n^{-\frac{c_s}{2d\gamma}}\right).$$

Corollary 13 decomposes the error into a regression component (dependent on m and h) and a distributional approximation component (dependent on the Hilbert map convergence rate from Theorem 9). This explicit rate characterization highlights the trade-off between the sample size of predictors and the internal complexity of the distribution-valued responses.

V. SIMULATION

We evaluate the proposed HiMAP methodology in two complementary settings. First, we benchmark the *HiMAP barycenter* against two widely used OT surrogates, *Sliced WB* and *Sinkhorn WB*, to illustrate the qualitative form of the HiMAP barycenter and its computational profile (Figs. 4–5). Second, we study the downstream impact in distribution-valued Fréchet regression by comparing HiMAP-based regression with the method of [31] (FM).

A. Barycenter benchmarks

All benchmarks in this subsection use empirical measures with uniform point masses. All three methods output free-support barycenters with the same number of support points as the inputs, allowing direct visual comparison. Since the three approaches optimize different objectives, with HiMAP operating in the quantile-induced geometry, Sliced WB being projection-based, and Sinkhorn WB being entropic-regularized OT, we aim to demonstrate that HiMAP yields barycenters qualitatively comparable to standard OT surrogates, while offering significant computational advantages.

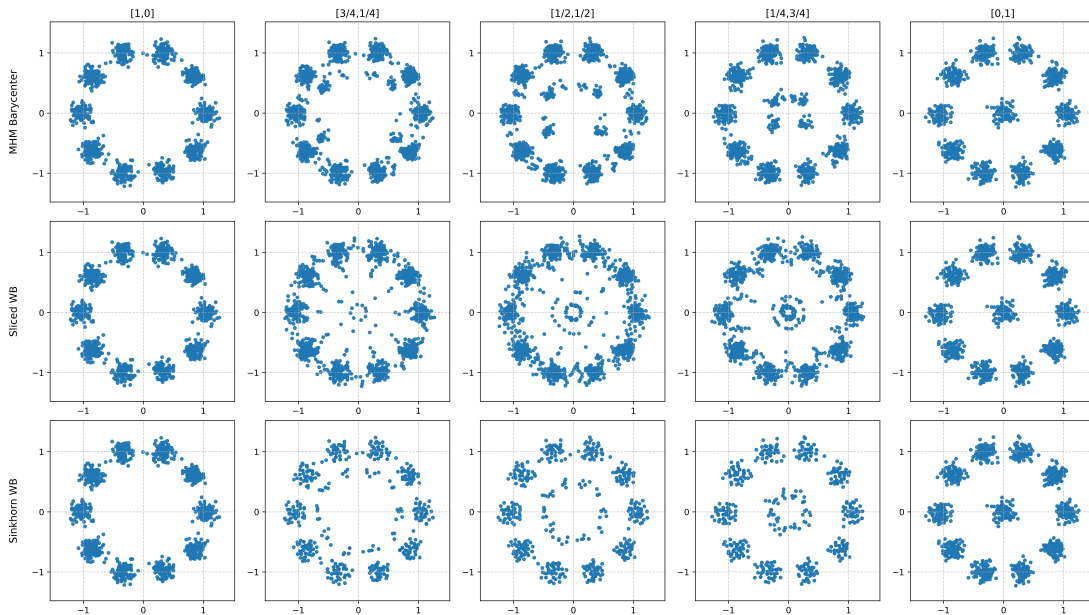


Fig. 4. Barycentric interpolation between two clustered measures. Columns correspond to weights $[1, 0]$, $[3/4, 1/4]$, $[1/2, 1/2]$, $[1/4, 3/4]$, and $[0, 1]$. Rows show the HiMAP Barycenter (top), Sliced WB (middle), and Sinkhorn WB (bottom).

Barycentric interpolation between clustered measures: We first study barycentric interpolation between two clustered distributions in \mathbb{R}^2 . The left distribution consists of 10 Gaussian clusters positioned on a ring, while the right distribution contains the same 10 ring clusters plus one additional central cluster. To ensure a fair free-support comparison, both measures contain 1100 support points: 10×110 points for the ring clusters (left) and 11×100 points per cluster including the central one (right). We compute barycenters for the weights

$$w \in \left\{ [1, 0], \left[\frac{3}{4}, \frac{1}{4}\right], \left[\frac{1}{2}, \frac{1}{2}\right], \left[\frac{1}{4}, \frac{3}{4}\right], [0, 1] \right\},$$

where $[1, 0]$ and $[0, 1]$ recover the two endpoints.

Fig. 4 shows that across intermediate weights, all three methods retain a prominent ring structure while gradually reallocating mass toward the center, reflecting the additional central mode in the right-hand measure. Despite using different geometric mechanisms, the interpolants are visually comparable at this scale, illustrating that HiMAP can serve as a lightweight barycentric operator for multivariate distribution interpolation.

Barycenter of nested ellipses: We next consider aggregation of 30 distributions supported on nested ellipses. Each distribution is generated by sampling points on two ellipses (outer and inner) with random centers, random semi-axes, and independent random rotations. Each empirical measure contains 1000 support points, and we compute the barycenter under uniform weights $w_i = 1/30$ for $i = 1, \dots, 30$.

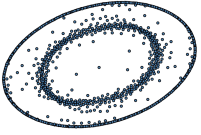
Concentric Ellipses	Method	MHM Barycenter	Sliced WB	Sinkhorn WB
	Barycenter			
	Time	0.028 s	11.366 s	301.078 s
	EMD	0.304	0.301	0.318

Fig. 5. Concentric ellipses benchmark with 30 input measures (left block). We compare the HiMAP Barycenter, Sliced WB, and Sinkhorn WB. Reported are the barycenter point clouds (top row within the table), the runtime (seconds), and the average unregularized OT cost to the inputs under uniform weights.

Fig. 5 reports barycenter point clouds and wall-clock runtime. In this benchmark, HiMAP completes in 0.028 s, compared to 11.366 s for Sliced WB and 301.078 s for Sinkhorn WB. HiMAP achieves a substantial runtime reduction while producing a barycenter that is visually comparable to both baselines. To provide a common quantitative proxy across methods, we also report the average unregularized OT cost $\sum_{i=1}^{30} w_i \text{OT}(\hat{\nu}, \nu_i)$ computed by discrete EMD with uniform masses; the resulting costs are of similar magnitude across methods.

B. Fréchet regression via HiMAP barycenters

We now assess how HiMAP performs as the barycentric subroutine in downstream Fréchet regression, where weights are affine and repeated barycenter evaluations are required. We compare against FM [31], which performs regression via Sinkhorn-based transport computations on a discretized grid and addresses affine weights by regressing optimal transport maps in a tangent space relative to a reference distribution.

Bivariate global Fréchet regression: comparison with FM: We consider distribution-valued response supported on dimension $p = 2$ and draw $X \sim \text{Unif}[0, 1]$. The conditional distributional trajectory is given by

$$Y | X = x \sim \mathcal{N}\left(\begin{pmatrix} 0.4x + 0.3 \\ 0.4x + 0.3 \end{pmatrix}^\top, \Sigma(x)\right),$$

with $\Sigma(x) = V\Lambda V^\top$, where $V = \frac{\sqrt{2}}{2} \begin{pmatrix} 1 & 1 \\ -1 & 1 \end{pmatrix}$, $\Lambda = \text{diag}(\lambda_1, \lambda_2)$, and $(\lambda_1, \lambda_2) | X = x \sim \frac{1}{100} \mathcal{N}\left(\begin{pmatrix} 1 + 0.5x \\ 1 - 0.5x \end{pmatrix}^\top, 0.01I_2\right)$.

For each Monte Carlo replicate, we generate $m = 101$ covariate values uniformly spaced over $[0, 1]$. A subset of 51 points $\{x_1, x_3, \dots, x_{99}, x_{101}\}$ is treated as observed points for model fitting, and the remaining 50 points are reserved for out-of-sample prediction. At each observed covariate value, the distribution-valued response is approximated by an empirical measure constructed from $n = 10^5$ i.i.d. draws. In the FM implementation, we use 51 grid points along each marginal (hence $51 \times 51 = 2601$ grid locations for each bivariate distribution). The simulation is repeated independently 50 times.

TABLE II
 RUNTIME AND ESTIMATION ACCURACY FOR GLOBAL FRÉCHET REGRESSION. REPORTED VALUES ARE THE MEAN (STANDARD DEVIATION) OVER 50 MONTE CARLO REPLICATES.

Method	MISE ($\times 10^{-4}$)	Time (s)
FM	8.39 (0.35)	369.64 (25.03)
HiMAP	5.59 (0.08)	3.70 (0.31)

Estimation accuracy is quantified by the mean integrated Sinkhorn error (MISE): for the k th replicate,

$$\text{MISE}_k = \int_0^1 W_{2,\epsilon}^2(\hat{\mu}_G^{(k)}(x), \mu_G(x)) dx,$$

where $W_{2,\epsilon}$ denotes the Sinkhorn-regularized Wasserstein distance with entropic parameter ϵ .

Table II shows that HiMAP achieves a substantial speed-up while also improving estimation accuracy. In particular, the average runtime is reduced by roughly two orders of magnitude relative to FM, with smaller and more stable MISE across replicates.

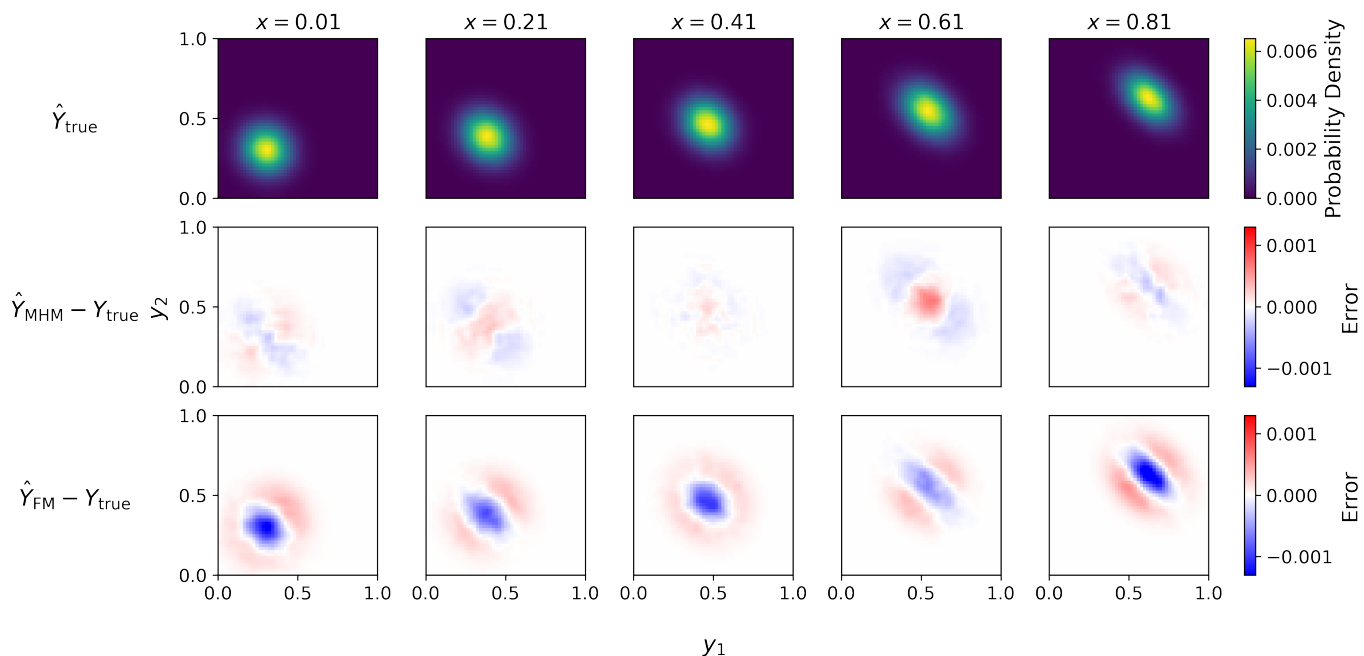


Fig. 6. Ground-truth and estimated distributions for different values of the covariate x . The first row shows the ground-truth distributions. The second and third rows display the prediction errors of the HiMAP and FM estimates relative to the truth, respectively. All error plots share the same color scale.

Fig. 6 provides a representative visual comparison: across covariate values, the discrepancy maps produced by HiMAP are generally weaker in magnitude and more concentrated, whereas FM exhibits more pronounced error patterns, consistent with the quantitative results.

Scalability: higher dimensions and local regression: To further assess scalability, we extend the experiments to response dimensions $p \in \{2, 5\}$ and consider both global and local Fréchet regression. We sample $X \sim \text{Unif}[-0.5, 0.5]$ and generate $Y | X = x \sim \mathcal{N}(\mu(x), \Sigma(x))$ with $\Sigma(x) = V\Lambda(x)V^\top$, where $V \in \mathbb{R}^{p \times p}$ is a randomly generated orthonormal matrix. Here $\mu(x) | X = x \sim \mathcal{N}(\alpha(x), 0.01I_p)$ and $\lambda(x) | X = x \sim \mathcal{N}(\beta(x), 0.01I_p)$ determine $\Lambda(x) = \text{diag}\{\lambda_1(x), \dots, \lambda_p(x)\}$. The specific settings are summarized in Table III. In each configuration, we use sample sizes $m \in \{50, 100, 200\}$ and set $n = 10^5$ samples per distribution. Accuracy is evaluated by the same MISE criterion.

Table IV reinforces that HiMAP delivers both competitive accuracy and a substantial computational advantage over the FM baseline. In the bivariate ($p = 2$) experiments, under both global and local Fréchet regression, HiMAP consistently attains smaller MISE than FM, indicating that it estimates the target regression barycenters reliably across the three sample-size settings. Meanwhile, the runtime gap is large and stable: HiMAP completes in a few seconds, whereas FM typically requires hundreds to over a thousand seconds, amounting to an almost two orders of magnitude speed-up.

Beyond $p = 2$, Table IV also highlights the practical feasibility of HiMAP in higher dimensions. We omit FM for $p = 5$ because its grid-based discretization scales exponentially with the response dimension (e.g., 50^5 grid cells for $p = 5$), quickly becoming prohibitive in both memory and runtime, whereas HiMAP remains computationally tractable. Even when the response

TABLE III
SPECIFIC SIMULATION SETTINGS.

Dimension	Regression	Setting
$p = 2$	Global	$\alpha(x) = (x, x)^\top$, $\beta(x) = \text{diag}(x + 1, x + 1)$
	Local	$\alpha(x) = \frac{1}{2}(\sin(2\pi x), \sin(2\pi x))^\top$, $\beta(x) = \text{diag}(\cos(0.9\pi x), \cos(0.9\pi x))$
$p = 5$	Global	$\alpha(x) = (x, \dots, x)^\top$, $\beta(x) = \text{diag}(x + 1, \dots, x + 1)$
	Local	$\alpha(x) = \frac{1}{2}(\sin(2\pi x), \dots, \sin(2\pi x))^\top$, $\beta(x) = \text{diag}(\cos(0.9\pi x), \dots, \cos(0.9\pi x))$

TABLE IV
ESTIMATION ACCURACY AND RUNTIME UNDER DIFFERENT SIMULATION CONFIGURATIONS AND SAMPLE SIZES m .

Dimension	Regression	m	HiMAP		FM	
			MISE ($\times 10^{-3}$)	Time (s)	MISE ($\times 10^{-3}$)	Time (s)
$p = 2$	Global	50	7.132	3.99	7.409	326.32
		100	7.216	7.85	7.519	816.91
		200	7.329	15.99	7.616	1303.81
	Local	50	9.784	4.00	10.130	437.21
		100	9.903	7.99	10.251	706.00
		200	9.332	15.58	9.675	1527.10
$p = 5$	Global	50	6.988	7.09	–	–
		100	7.047	13.72	–	–
		200	7.049	26.91	–	–
	Local	50	9.499	6.83	–	–
		100	9.308	13.47	–	–
		200	8.144	27.35	–	–

dimension increases to $p = 5$, HiMAP continues to achieve low estimation error under both global and local regression, and the runtime remains on the order of seconds (tens of seconds at the largest m considered).

Overall, HiMAP provides an efficient and accurate barycenter-based Fréchet regression procedure. It yields substantial speed-ups while preserving, and often improving, estimation accuracy relative to FM. These gains are particularly notable given that FM already relies on an explicit discretization to accelerate computation, whereas HiMAP operates directly on the observed samples. Moreover, HiMAP remains effective as the response dimension increases, making it suitable for genuinely multivariate distributional regression problems.

VI. REAL DATA ANALYSIS

We illustrate the practical relevance of HiMAP in multivariate climate-indicator data. In climate adaptation and risk assessment, it is often the *full distribution* of climatic conditions, including tails and cross-variable dependence, that is operationally important, rather than a few moment summaries. Month-specific climate distributions can therefore differ in ways that go beyond shifts in mean and variance, making distribution-valued modeling a natural choice.

Data and distributional representation: We use the Copernicus Climate Data Store dataset *Climate indicators for Europe from 1940 to 2100 derived from reanalysis and climate projections**, and focus on the reanalysis period 1940–2024. For Greece, we extract five monthly indicators: mean temperature, growing degree days, total precipitation, maximum consecutive five-day precipitation, and mean wind speed. For each calendar month $j \in \{1, \dots, 12\}$, we collect one p -dimensional observation per year over 1940–2024, yielding $n = 84$ vectors $\{Z_{j\ell}\}_{\ell=1}^n \subset \mathbb{R}^p$ with $p = 5$. The month-specific empirical measure

$$\hat{\mu}_j = \frac{1}{n} \sum_{\ell=1}^n \delta_{Z_{j\ell}}$$

serves as the observed *climate distribution* for month j , capturing the joint behavior of the indicators across years within that month. To provide an interpretable visualization, we first focus on the two key indicators (monthly mean temperature and

*<https://cds.climate.copernicus.eu/datasets/sis-ecde-climate-indicators?tab=download>

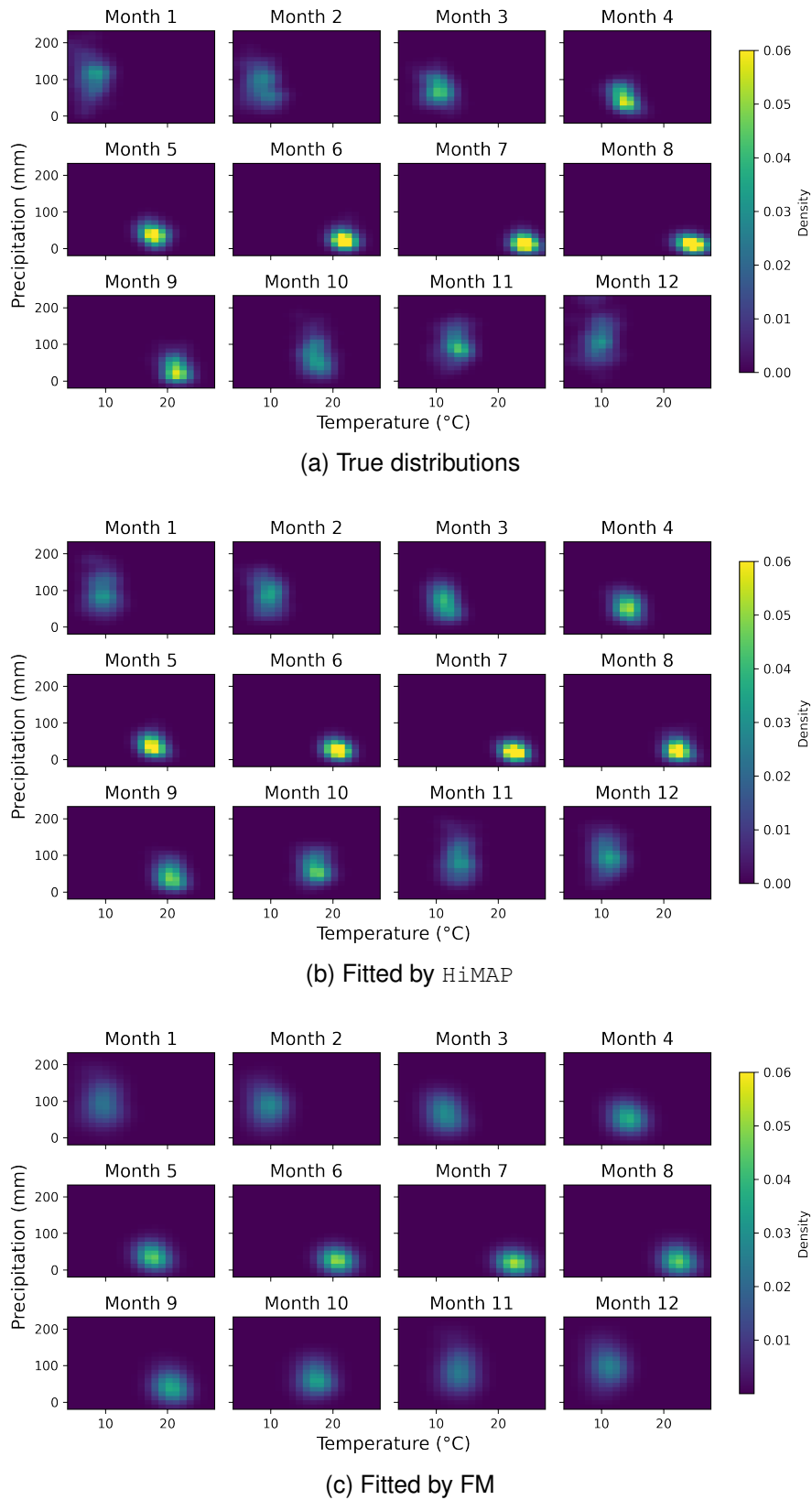


Fig. 7. Monthly climate distributions of temperature and precipitation over 1940–2024 for Greece. Panel (a) shows the empirical distribution for each month, and panels (b)–(c) show the corresponding two-dimensional leave-one-month-out regression fits obtained by HiMAP and FM, respectively.

total precipitation) and consider the induced bivariate marginal distributions; Figure 7(a) shows these empirical distributions for Greece.

Regression setup and evaluation: We treat the month index as the predictor, $X = j$, with distribution-valued response $Y(X) = \hat{\mu}_j$, and fit a local Fréchet regression model using the HiMAP barycenter operator from Section IV. Predictive performance is assessed via a leave-one-month-out protocol: for each month j , we refit the model on the remaining 11 months and predict at $X = j$, then evaluate the prediction error using the same MISE criterion as in Section V-B.

Two-dimensional fits: HiMAP versus FM: Figures 7(b)–(c) compare the fitted month-wise bivariate distributions produced by HiMAP and by the FM baseline, respectively. Both approaches recover the expected Mediterranean seasonal pattern, with hot, dry summers with low precipitation and higher temperatures, and milder, wetter winters, visible as a systematic migration of the joint distribution across the annual cycle (Figure 7(a)). Quantitatively, under leave-one-out the MISE values are 3.14×10^{-3} for HiMAP and 3.38×10^{-3} for FM, indicating that HiMAP yields predictive accuracy comparable to a standard OT-based baseline. At the same time, HiMAP is substantially more efficient: the total runtime for the leave-one-out analysis is approximately 0.02 seconds for HiMAP versus about 80 seconds for FM. This gap is consistent with the algorithmic structure emphasized in Sections III–IV, namely that HiMAP reduces regression to explicit operations in an L^2 representation without iterative OT solvers.

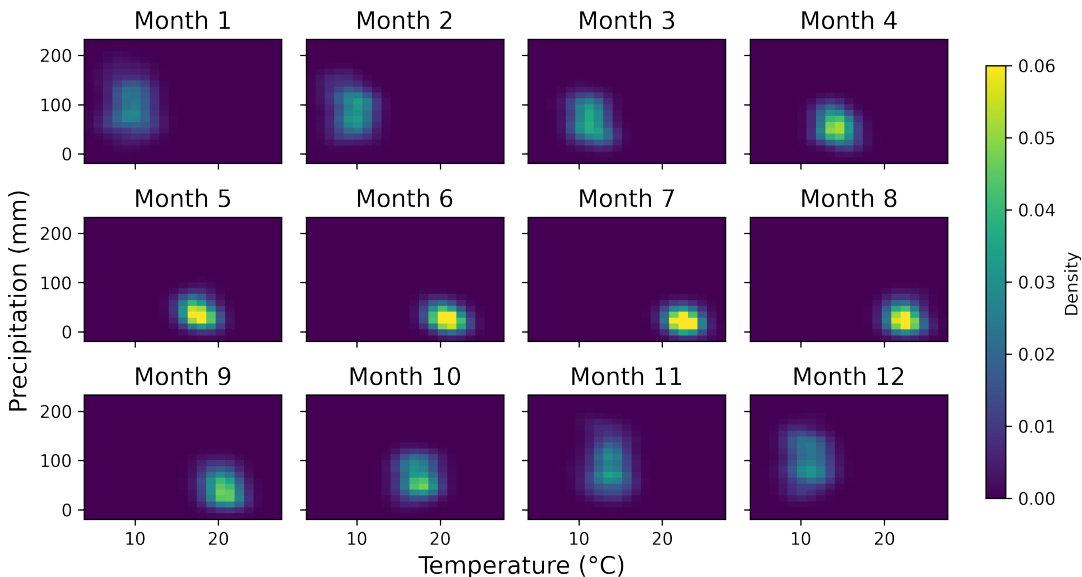


Fig. 8. Greece ($p = 5$): fitted monthly climate distributions obtained by HiMAP using all five indicators over 1940–2024 (visualized in the temperature–precipitation plane).

Five-dimensional fits: direct multivariate regression: We further apply HiMAP to the full set of five indicators ($p = 5$) without dimension reduction. Figure 8 shows the corresponding fitted results (projected to temperature and precipitation for visualization). Under the same leave-one-out protocol, the MISE is 3.1×10^{-3} . This experiment underscores the scalability of HiMAP for genuinely multivariate distributional regression: the method remains directly applicable in higher dimensions, while baselines that rely on grid-based discretization become increasingly restrictive as p grows.

To further illustrate the stability of our method beyond the Greece example, we report additional results for four countries: Norway, Spain, the United Kingdom, and Poland. For each country, we show the true monthly distributions of different climate indicators and the corresponding fitted results obtained by HiMAP in Fig. 9–12.

Overall, these additional examples exhibit diverse seasonal patterns across countries and indicator pairs. For instance, Norway shows strong seasonality in temperature with winter-dominated precipitation, while Spain tends to display drier summers and more concentrated precipitation in cooler months. The United Kingdom and Poland present comparatively milder seasonal temperature variation, but distinct month-to-month changes in precipitation-related extremes. In all cases, HiMAP closely tracks the evolution of the monthly distributions and produces fitted results that are consistent with the observed seasonal structure.

VII. CONCLUSION

We proposed the Hilbert mass-aligned parameterization (HiMAP) to enable tractable barycentric aggregation and distribution-valued Fréchet regression for multivariate probability measures. By replacing purely geometric space-partitions with equiprobable conditional-median splits along a Hilbert-type recursion, HiMAP induces a distribution-invariant mass coordinate $t \in [0, 1]$ and a quantile-map representation Q_μ that embeds $\mathcal{P}_\infty(\mathbb{R}^d)$ into an L^2 space. A key consequence is linear closure under affine

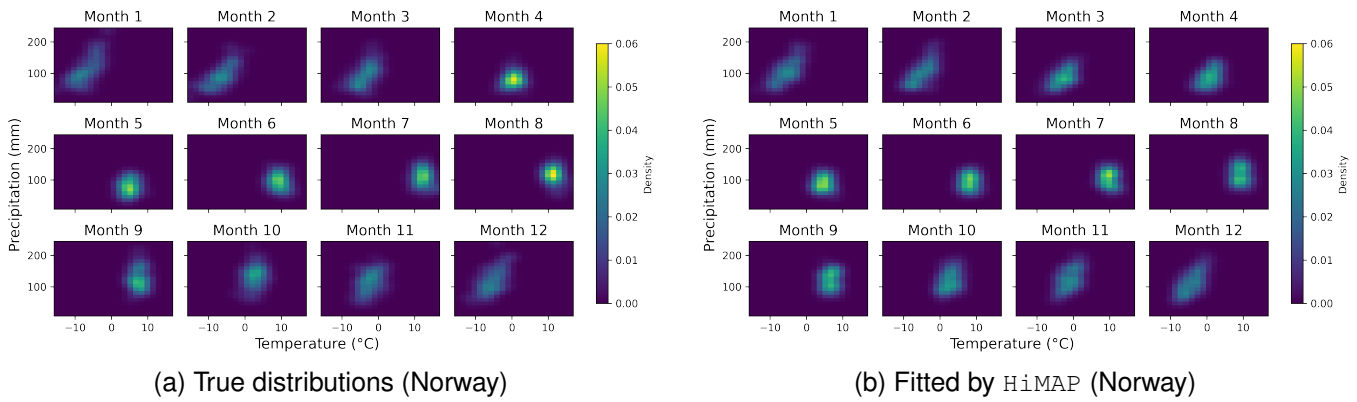


Fig. 9. Norway: true and HiMAP-fitted monthly climate distributions of mean temperature and total precipitation. The HiMAP achieves an MISE of 2.6×10^{-3} .

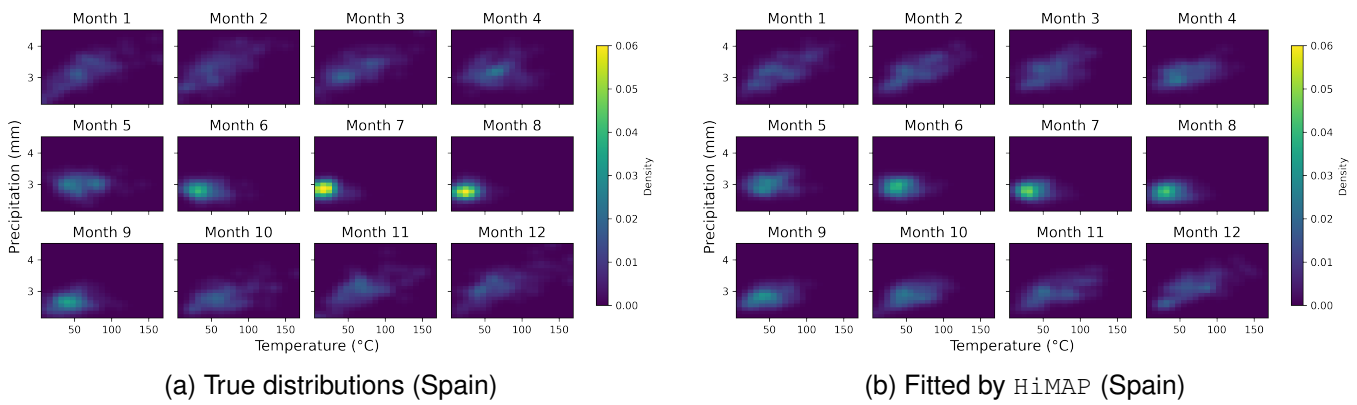


Fig. 10. Spain: true and HiMAP-fitted monthly climate distributions of total precipitation and wind speed. The HiMAP achieves an MISE of 2.3×10^{-3} .

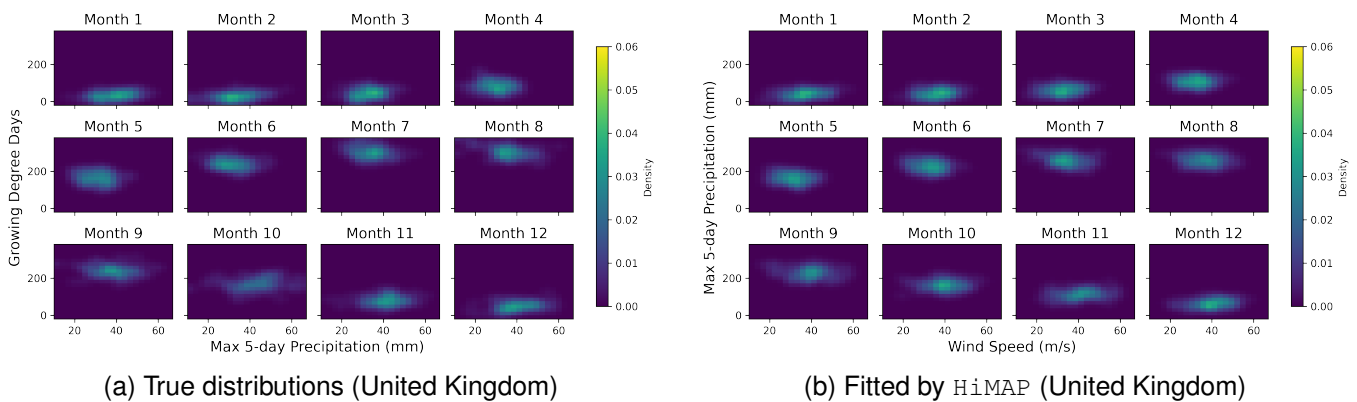


Fig. 11. United Kingdom: true and HiMAP-fitted monthly climate distributions of max 5-day precipitation and growing degree days. The HiMAP achieves an MISE of 1.8×10^{-3} .

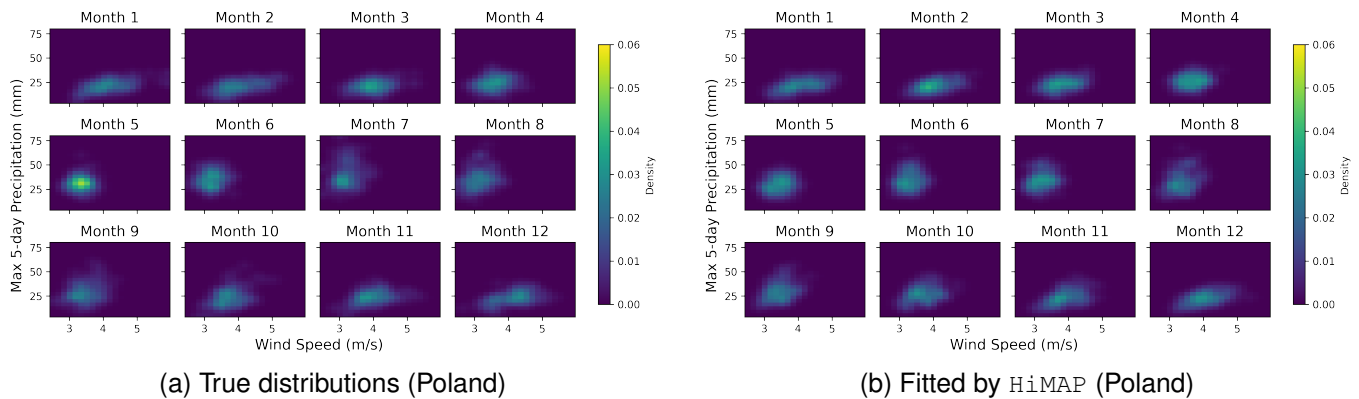


Fig. 12. Poland: true and HiMAP-fitted monthly climate distributions of wind speed and max 5day precipitation. The HiMAP achieves an MISE of 1.9×10^{-3} .

combinations of quantile functions, which yields a well-posed HiMAP barycenter operator for signed weights (after normalization) and makes Fréchet regression explicit as a weighted average in the representation space, together with corresponding consistency and convergence guarantees for empirical estimators.

Empirically, HiMAP is non-iterative and particularly advantageous in regimes that require many barycenter evaluations. Across controlled barycenter diagnostics, regression simulations, and a multivariate climate-indicator study, HiMAP produces barycenters and regression fits that are qualitatively comparable to standard OT surrogates while offering substantial speed-ups. Future work includes extending the theory beyond $\mathcal{P}_\infty(\mathbb{R}^d)$, developing data-adaptive splitting/orientation policies for anisotropic measures, and refining asymptotic results for regression functionals under additional structural assumptions.

REFERENCES

- [1] A. Petersen, X. Liu, and A. A. Divani, “Wasserstein f-tests and confidence bands for the fréchet regression of density response curves,” *The Annals of Statistics*, vol. 49, no. 1, pp. 590–611, 2021.
- [2] Y. Chen, Z. Lin, and H.-G. Müller, “Wasserstein regression,” *Journal of the American Statistical Association*, vol. 118, no. 542, pp. 869–882, 2023.
- [3] C. Villani, *Optimal transport: old and new*. Springer, 2009, vol. 338.
- [4] V. M. Panaretos and Y. Zemel, “Statistical aspects of Wasserstein distances,” *Annual Review of Statistics and Its Application*, vol. 6, no. 1, pp. 405–431, 2019.
- [5] M. Agueh and G. Carlier, “Barycenters in the Wasserstein space,” *SIAM Journal on Mathematical Analysis*, vol. 43, no. 2, pp. 904–924, 2011.
- [6] A. Petersen and H.-G. Müller, “Fréchet regression for random objects with Euclidean predictors,” *The Annals of Statistics*, vol. 47, no. 2, pp. 691–719, 2019.
- [7] L. Lin, W. Shi, J. Ye, and J. Li, “Multisource single-cell data integration by MAW barycenter for Gaussian mixture models,” *Biometrics*, vol. 79, no. 2, pp. 866–877, 2023.
- [8] M. K. Chung, C. Garcia Ramos, F. Branco De Paiva, J. Mathis, V. Prabhakaran, V. A. Nair, M. E. Meyerand, B. P. Hermann, J. R. Binder, and A. F. Struck, “Unified topological inference for brain networks in temporal lobe epilepsy using the Wasserstein distance,” *NeuroImage*, vol. 284, p. 120436, 2023.
- [9] T. Wang, M. Li, G. Zeng, C. Meng, and Q. Zhang, “Gaussian herding across pens: An optimal transport perspective on global Gaussian reduction for 3DGS,” *arXiv preprint arXiv:2506.09534*, 2025.
- [10] Y. Wang, Y. Li, Q. Yang, and H. Ding, “Finding Wasserstein Ball Center: Efficient algorithm and the applications in fairness,” in *Proceedings of the 42nd International Conference on Machine Learning*, ser. Proceedings of Machine Learning Research, vol. 267, 2025, pp. 63490–63515.
- [11] G. Peyré and M. Cuturi, “Computational optimal transport: With applications to data science,” *Foundations and Trends in Machine Learning*, vol. 11, no. 5-6, pp. 355–607, 2019.
- [12] M. Cuturi, “Sinkhorn distances: Lightspeed computation of optimal transport,” in *Advances in Neural Information Processing Systems*, vol. 26, 2013, pp. 2292–2300.
- [13] A. Genevay, M. Cuturi, G. Peyré, and F. Bach, “Stochastic optimization for large-scale optimal transport,” in *Advances in Neural Information Processing Systems*, vol. 29, 2016.
- [14] J. Altschuler, J. Weed, and P. Rigollet, “Near-linear time approximation algorithms for optimal transport via Sinkhorn iteration,” in *Advances in Neural Information Processing Systems*, vol. 30, 2017.
- [15] J. Altschuler, F. Bach, A. Rudi, and J. Niles-Weed, “Massively scalable Sinkhorn distances via the Nyström method,” in *Advances in Neural Information Processing Systems*, vol. 32, 2019.
- [16] P. Dvurechensky, A. Gasnikov, and A. Kroshnin, “Computational optimal transport: Complexity by accelerated gradient descent is better than by Sinkhorn’s algorithm,” in *Proceedings of the 35th International Conference on Machine Learning*, ser. Proceedings of Machine Learning Research, vol. 80, 2018, pp. 1367–1376.
- [17] A. Thibault, L. Chizat, C. Dossal, and N. Papadakis, “Overrelaxed Sinkhorn–Knopp algorithm for regularized optimal transport,” *Algorithms*, vol. 14, no. 5, p. 143, 2021.
- [18] M. Li, J. Yu, T. Li, and C. Meng, “Importance sparsification for Sinkhorn algorithm,” *Journal of Machine Learning Research*, vol. 24, no. 247, pp. 1–44, 2023.
- [19] J. Ye, P. Wu, J. Z. Wang, and J. Li, “Fast discrete distribution clustering using Wasserstein barycenter with sparse support,” *IEEE Transactions on Signal Processing*, vol. 65, no. 9, pp. 2317–2332, 2017.
- [20] K. C. Cheng, S. Aeron, M. C. Hughes, and E. L. Miller, “Nonparametric and regularized dynamical Wasserstein barycenters for sequential observations,” *IEEE Transactions on Signal Processing*, vol. 71, pp. 3164–3178, 2023.
- [21] P. Cisneros-Velarde and F. Bullo, “Distributed Wasserstein barycenters via displacement interpolation,” *IEEE Transactions on Control of Network Systems*, vol. 10, no. 2, pp. 785–795, 2023.

- [22] N. Bonneel, J. Rabin, G. Peyré, and H. Pfister, “Sliced and Radon Wasserstein barycenters of measures,” *Journal of Mathematical Imaging and Vision*, vol. 51, no. 1, pp. 22–45, 2015.
- [23] I. Deshpande, Y.-T. Hu, R. Sun, A. Pyrros, N. Siddiqui, S. Koyejo, Z. Zhao, D. Forsyth, and A. G. Schwing, “Max-sliced Wasserstein distance and its use for GANs,” in *Proceedings of the IEEE/CVF Conference on Computer Vision and Pattern Recognition*, 2019, pp. 10 648–10 656.
- [24] S. Kolouri, K. Nadjahi, U. Simsekli, R. Badeau, and G. Rohde, “Generalized sliced Wasserstein distances,” in *Advances in Neural Information Processing Systems*, vol. 32, 2019.
- [25] T. Le, M. Yamada, K. Fukumizu, and M. Cuturi, “Tree-sliced variants of Wasserstein distances,” in *Advances in Neural Information Processing Systems*, vol. 32, 2019.
- [26] T. Lin, C. Fan, N. Ho, M. Cuturi, and M. I. Jordan, “Projection robust Wasserstein distance and Riemannian optimization,” in *Advances in Neural Information Processing Systems*, vol. 33, 2020.
- [27] T. Li, J. Yu, and C. Meng, “Scalable model-free feature screening via sliced-Wasserstein dependency,” *Journal of Computational and Graphical Statistics*, vol. 32, no. 4, pp. 1501–1511, 2023.
- [28] T. Li, C. Meng, H. Xu, and J. Zhu, “Efficient variants of Wasserstein distance in hyperbolic space via space-filling curve projection,” *IEEE Transactions on Neural Networks and Learning Systems*, 2025.
- [29] C. Meng, Y. Ke, J. Zhang, M. Zhang, W. Zhong, and P. Ma, “Large-scale optimal transport map estimation using projection pursuit,” in *Advances in Neural Information Processing Systems*, vol. 32, 2019.
- [30] J. Zhang, W. Zhong, and P. Ma, “A review on modern computational optimal transport methods with applications in biomedical research,” in *Modern Statistical Methods for Health Research*. Springer, 2021, pp. 279–300.
- [31] J. Fan and H.-G. Müller, “Conditional Wasserstein barycenters and interpolation/extrapolation of distributions,” *IEEE Transactions on Information Theory*, vol. 71, no. 5, pp. 3835–3853, 2025.
- [32] J. Weed and F. Bach, “Sharp asymptotic and finite-sample rates of convergence of empirical measures in Wasserstein distance,” *Bernoulli*, vol. 25, no. 4A, pp. 2620–2648, 2019.
- [33] H. Sagan, *Space-Filling Curves*. Springer, 1994.
- [34] A. W. Van Der Vaart and J. A. Wellner, “Weak convergence,” in *Weak convergence and empirical processes: with applications to statistics*. Springer, 1996, pp. 16–28.

APPENDIX A
DETAILED HILBERT CURVE CONSTRUCTION

This appendix makes explicit the ‘‘Hilbert ordering rules’’ used throughout Section III-A–III-C to associate each $t \in [0, 1]$ with a nested sequence of cells $\{\mathcal{B}_\ell(t)\}_{\ell \geq 0}$. We present the construction from a discrete, implementation-oriented viewpoint, and clarify the relation between the classical k -order Hilbert curve and our binary splitting depth L , as well as its adaptation to finite empirical samples.

a) k -order Hilbert curve versus binary depth L : The classical k -order Hilbert construction partitions a d -dimensional hypercube into $(2^k)^d = 2^{dk}$ congruent subcubes, and traverses them in a continuous, locality-preserving order. In contrast, our mass-aligned recursion in Section III-A performs *binary* splits sequentially along coordinates according to the schedule $s(\ell) \in \{1, \dots, d\}$, producing 2^L terminal cells after L splits. Under a balanced/cyclic schedule (e.g. $s(\ell) = 1 + ((\ell - 1) \bmod d)$), every block of d consecutive splits refines each coordinate once; hence one may regard

$$L \approx dk \quad (\text{exactly } L = dk \text{ when } L \text{ is a multiple of } d \text{ under the cyclic schedule}). \quad (9)$$

This is the sense in which our depth- L tree corresponds to a k -order Hilbert refinement: $k = \lfloor L/d \rfloor$ full ‘‘Hilbert macro-levels’’ plus a remainder of $L - d\lfloor L/d \rfloor$ additional binary splits.

b) From t to a discrete Hilbert address: Fix an order $k \geq 1$ and define $M_k := 2^{dk}$. Ignoring a null set of t with non-unique base expansions, the standard way to select the k -level cell visited by the Hilbert curve at parameter t is to take the *discrete Hilbert index*

$$h_k(t) := \lfloor t M_k \rfloor \in \{0, 1, \dots, M_k - 1\}. \quad (10)$$

Equivalently, expand t in base 2^d :

$$t = \sum_{r=1}^{\infty} \frac{\alpha_r}{(2^d)^r}, \quad \alpha_r \in \{0, 1, \dots, 2^d - 1\}, \quad (11)$$

and use the first k digits $(\alpha_1, \dots, \alpha_k)$; this k -tuple is precisely the base- (2^d) representation of $h_k(t)$. Each digit α_r specifies *which* of the 2^d subcells is entered at macro-level r , *after* accounting for the current Hilbert orientation (state) at that level.

c) Orientation and why reflections appear (2D illustration): For $d = 2$, each macro-level divides a square into four quadrants. The Hilbert order is not a fixed lexicographic order: to keep the curve continuous, the local traversal inside certain quadrants must be rotated/reflected. This is exactly the ‘‘reflection before recursing’’ rule illustrated by many discrete Hilbert-sort explanations: in the default orientation, the lower-left (LL) quadrant is reflected across its main diagonal before recursing, and the lower-right (LR) quadrant is reflected across its anti-diagonal. Figure 13 redraws these two reflection operations in a compact form.

Algorithmically, these geometric reflections manifest as a *permutation of the splitting axes* and a *flip in the sorting direction* (e.g., swapping logical x and y axes and reversing the greater/less-than comparator). This explicit axis swapping is the exact mechanism that causes a scheduled logical x -split to map to a geometric y -split in the global coordinate system for specific sub-quadrants, maintaining spatial continuity without violating the recursive binary tree structure.

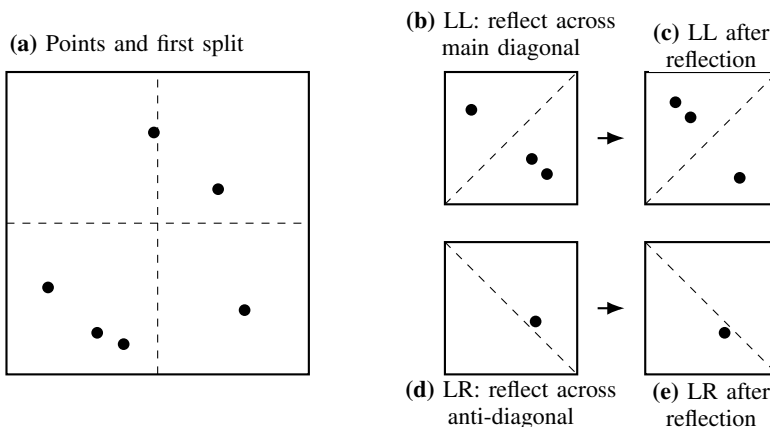


Fig. 13. Reflections used by the 2D discrete Hilbert recursion (schematic). In the default orientation, the LL quadrant is reflected across its main diagonal and the LR quadrant across its anti-diagonal before recursing. These reflections are the geometric manifestation of the orientation/state updates in standard Hilbert indexing.

d) “Given t , which k -order subcell is selected?” (2D worked logic): For $d = 2$, write the base-4 expansion $t = \sum_{r \geq 1} \alpha_r 4^{-r}$ as in (11) (here $2^d = 4$). At order k , the prefix $(\alpha_1, \dots, \alpha_k)$ determines a unique depth- k sub-square. Concretely, α_1 chooses one of the four quadrants in the order induced by the current orientation; then inside that chosen quadrant, α_2 chooses one of its four sub-quadrants, again after applying the appropriate local reflection/rotation dictated by the quadrant type (LL/LR require reflections as in Figure 13); continuing for k steps yield the final k -order cell.

Figure 14 visualizes this address interpretation for $k = 2$: the first digit α_1 selects the macro-quadrant, and the second digit α_2 selects the sub-quadrant, with LL/LR using mirrored local orders due to the required reflections.

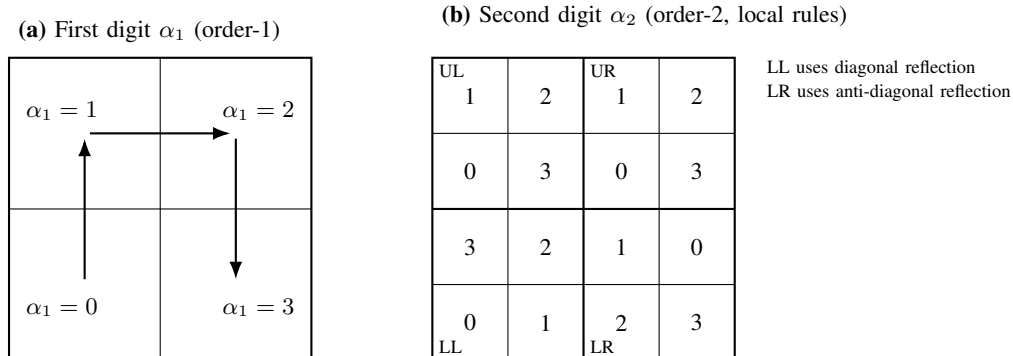


Fig. 14. Discrete address view for $d = 2$, $k = 2$. The base-4 digits $t = \sum_{r \geq 1} \alpha_r 4^{-r}$ select nested cells. The first digit α_1 picks the order-1 quadrant; the second digit α_2 picks the sub-quadrant inside it, with LL/LR using mirrored local orders due to the required reflections.

e) *How this produces $\{\mathcal{B}_\ell(t)\}$ in our mass-aligned tree:* In the classical geometry-driven Hilbert curve, the k -level cell is a fixed dyadic subcube of side length 2^{-k} . In our HiMAP construction, the *ordering* of sibling cells follows the same Hilbert recursion, but the *cell boundaries* are determined by conditional medians as in (2)–(3). Operationally, once the digit sequence (or equivalently $h_k(t)$) identifies the intended child at each macro-level, we translate that choice into the corresponding sequence of d binary decisions along the schedule $s(\ell)$. Thus, for $k = \lfloor L/d \rfloor$, the first dk splits specify a depth- dk cell $\mathcal{B}_{dk}(t)$ consistent with the Hilbert order, and any remaining $\ell - dk$ splits refine it further to obtain $\mathcal{B}_L(t)$. This is exactly the “determine path indices (bits) based on t and Hilbert ordering rules” step in Algorithm 2.

f) *Adaptation to Finite Empirical Samples (Arbitrary n):* While the continuous formulation implicitly assumes an infinite resolution or perfectly balanced subsets, our practical implementation (Algorithm 2) inherently accommodates arbitrary empirical sample sizes n . Instead of enforcing a rigid grid, the recursion utilizes adaptive integer arithmetic to partition sample indices at the exact empirical median. If a sub-cell contains an odd number of points, the mass is divided as evenly as possible. Furthermore, if a sub-cell contains fewer points than required for a full d -dimensional macro-split (e.g., exactly two points remaining), the algorithm dynamically short-circuits the cyclic schedule and performs a single terminal binary split determined by the current local axis and orientation state. This guarantees that every empirical observation is assigned a unique, unambiguous Hilbert index without requiring synthetic data padding or causing algorithmic failure.

APPENDIX B ADDITIONAL NOTATION FOR PROOFS

This appendix consolidates auxiliary notation that is repeatedly used across the following proofs. Throughout, we work with $t \in [0, 1]$ that admits a unique Hilbert address (equivalently, excluding a Lebesgue-null set of dyadic endpoints).

(a) Hilbert addresses and dyadic interval partition. The Hilbert addressing rule (Appendix A) induces, for each depth L , a partition of $[0, 1]$ into 2^L half-open intervals $\{\mathcal{I}_L(\sigma) : \sigma \in \{0, 1\}^L\}$, each of Lebesgue measure 2^{-L} , such that σ encodes the first L branch decisions along the Hilbert recursion. Let \mathcal{N}_{end} denote the (countable) union of all interval endpoints across depths. For $t \in [0, 1] \setminus \mathcal{N}_{\text{end}}$, denote by $\sigma_L(t) \in \{0, 1\}^L$ the unique address satisfying $t \in \mathcal{I}_L(\sigma_L(t))$, and write $\sigma_l(t)$ for its length- l prefix.

(b) Path cells, cut points, and finite-depth maps. Recall the root cell $\mathcal{B}_0 = \mathcal{M} \cap \mathcal{S}$ from Section III-A. For $t \in [0, 1] \setminus \mathcal{N}_{\text{end}}$, the address $\{\sigma_l(t)\}_{l \geq 1}$ defines a nested sequence of *path cells* $\{\mathcal{B}_l(t)\}_{l \geq 0}$ by following the binary partition tree: $\mathcal{B}_l(t)$ is the $\sigma_l(t)$ -indexed depth- l descendant of \mathcal{B}_0 . We abbreviate the population conditional-median cut along the path by

$$q_l(t) := q_l(\mu; \mathcal{B}_{l-1}(t)) \quad (l \geq 1),$$

where $q_l(\mu; \cdot)$ is defined in (2). Recall $k_r(L) := \max\{l \leq L : s(l) = r\}$. The population finite-depth map and its limit are

$$\mathbf{H}_{\mu,L}(t) := (q_{k_1(L)}(t), \dots, q_{k_d(L)}(t))^\top, \quad \mathbf{Q}_\mu(t) := \lim_{L \rightarrow \infty} \mathbf{H}_{\mu,L}(t) \quad (\text{a.e. } t),$$

consistent with (4)–(5).

(c) Rectangle operations. We will use two rectangle operations. If $R = \prod_{r=1}^d [a_r, b_r]$ and $\lambda \in \mathbb{R}$, define

$$\lambda \odot R := \prod_{r=1}^d [\min(\lambda a_r, \lambda b_r), \max(\lambda a_r, \lambda b_r)]. \quad (12)$$

If $R = \prod_{r=1}^d [a_r, b_r]$ and $S = \prod_{r=1}^d [c_r, d_r]$, define

$$R \oplus S := \prod_{r=1}^d [a_r + c_r, b_r + d_r]. \quad (13)$$

(d) Interval representation of path cells and width shorthands. For each $l \geq 0$, write the (axis-aligned) box representation

$$\mathcal{B}_l(t) = \prod_{r=1}^d I_{l,r}(t), \quad I_{l,r}(t) = [L_{l,r}(t), U_{l,r}(t)], \quad |I_{l,r}(t)| = U_{l,r}(t) - L_{l,r}(t).$$

Let $j_l := s(l) \in \{1, \dots, d\}$ be the scheduled coordinate at depth l , and use the shorthand

$$|I_{s(l)}| := |I_{l-1, j_l}(t)| \quad (l \geq 1), \quad W_{\max} := \max_{1 \leq r \leq d} |I_{0,r}(t)|, \quad W_{\min} := \min_{1 \leq r \leq d} |I_{0,r}(t)|.$$

We also define $C_{\text{ratio}} := W_{\max}/W_{\min}$.

(e) Depth- L cut vectors, selection operator, and empirical counterparts. Stack the first L population cuts into

$$q^{(L)}(t) := (q_1(t), \dots, q_L(t))^\top \in \mathbb{R}^L.$$

Let $U_1, \dots, U_n \stackrel{i.i.d.}{\sim} \mu$, let P denote expectation under μ , and let P_n be the empirical measure. Let $\hat{q}^{(L)}(t)$ be the depth- L empirical cut vector returned by Algorithm 1 when traversing the t -path, and define

$$h_n^{(L)}(t) := \hat{q}^{(L)}(t) - q^{(L)}(t).$$

Define the $d \times L$ selection operator $D^{(L)}$ by

$$D^{(L)} q^{(L)}(t) = (q_{k_1(L)}(t), \dots, q_{k_d(L)}(t))^\top.$$

Then

$$\mathbf{H}_{\mu, L}(t) = D^{(L)} q^{(L)}(t), \quad \hat{\mathbf{Q}}_{\mu, L}(t) = D^{(L)} \hat{q}^{(L)}(t).$$

Finally, we define the scaling matrix

$$S_L := \text{diag}(|I_{s(1)}|, |I_{s(2)}|, \dots, |I_{s(L)}|).$$

(f) Density and geometry constants. Under Assumption 3(A.1), the density f of μ satisfies $0 < m \leq f \leq M < \infty$ on \mathcal{M} . We set

$$c_- := \frac{m}{M} \in (0, 1], \quad \alpha := \frac{m}{2M} \in \left(0, \frac{1}{2}\right], \quad \rho := 1 - \alpha = 1 - \frac{m}{2M} \in (0, 1),$$

so that (as in Lemma 4) each median split shrinks the chosen side length by at most a factor ρ .

(g) Score functions (recursive Z-estimation view). For each $l \geq 1$ and any $q^{(l)} \in \mathbb{R}^l$, define

$$\Psi_l(\mathbf{u}; q^{(l)}) := \mathbf{1}\{\mathbf{u} \in \mathcal{B}_{l-1}(q^{(l-1)})\} \left(\mathbf{1}\{u_{j_l} \leq q_l\} - \frac{1}{2} \right), \quad (14)$$

where $\mathcal{B}_{l-1}(q^{(l-1)})$ denotes the depth- $(l-1)$ box obtained by following the fixed t -address through the recursion while using the cut values $q^{(l-1)}$ (Appendix A governs the geometry/orientation rules). Stack

$$\Psi_{(L)}(\mathbf{u}; q^{(L)}) := (\Psi_1(\mathbf{u}; q^1), \dots, \Psi_L(\mathbf{u}; q^{(L)}))^\top \in \mathbb{R}^L.$$

By definition of conditional medians, $q^{(L)}(t)$ solves $P\Psi_{(L)}(\cdot; q^{(L)}(t)) = \mathbf{0}$, and $\hat{q}^{(L)}(t)$ solves $P_n\Psi_{(L)}(\cdot; \hat{q}^{(L)}(t)) = \mathbf{0}$.

(h) Hilbert-space notation used in barycenter proofs. Let

$$\mathcal{H} := L^2([0, 1]; \mathbb{R}^d), \quad \langle f, g \rangle_{\mathcal{H}} := \int_0^1 f(t)^\top g(t) dt, \quad \|f\|_{\mathcal{H}}^2 := \langle f, f \rangle_{\mathcal{H}}.$$

For $\nu \in \mathcal{P}_\infty(\mathbb{R}^d)$, write its HiMAP quantile function as $q_\nu(\cdot) := \mathbf{Q}_\nu(\cdot) \in \mathcal{H}$. For $\nu_i, \nu \in \mathcal{P}_\infty(\mathbb{R}^d)$, Proposition 8(ii) with $r = 2$ yields the identity

$$d_{\text{HiMAP}, 2}^2(\nu_i, \nu) = \int_0^1 \|q_{\nu_i}(t) - q_\nu(t)\|^2 dt = \|q_{\nu_i} - q_\nu\|_{\mathcal{H}}^2. \quad (15)$$

Given barycenter weights $\lambda_1, \dots, \lambda_q \in \mathbb{R}$, we further use the abbreviations

$$\Lambda := \sum_{i=1}^q \lambda > 0, \quad g := \sum_{i=1}^q \lambda_i q_{\nu_i} \in \mathcal{H}.$$

APPENDIX C PROOFS FOR SECTION III

A. Proof of Lemma 4

Proof of Lemma 4: Let current segment box \mathcal{B}_L be $\mathcal{B}_L = \prod_{j=1}^d I_j = \prod_{j=1}^d [L_{L,j}, U_{L,j}]$. The $s(L)$ -dim coordinate interval length is $\omega := |I_{s(L)}|$. Note the volume of the rest intervals is $V_{-s(L)} := \prod_{j \neq s(L)} |I_j|$. By our HiMAP construction, we will get two half-boxes $\mathcal{B}_L^+ := \mathcal{B}_L \cap \{u_{s(L)} < q_L\}$ and $\mathcal{B}_L^- := \mathcal{B}_L \cap \{u_{s(L)} \geq q_L\}$ with mass constraint,

$$\mu(\mathcal{B}_L^{(0)}) = \mu(\mathcal{B}_L^{(1)}) = \frac{1}{2}\mu(\mu(\mathcal{B}_L)).$$

Let $l^+ = |I_{s(L)} \cap \{-\infty, q_L\}|$, $l^- = \omega - l^+$, by Assumption 3,

$$\mu(\mathcal{B}_L) \in [m\omega V_{-s}, M\omega V_{-s}], \mu(\mathcal{B}_L^\pm) \in [ml^\pm V_{-s}, Ml^\pm V_{-s}].$$

By mass constraint,

$$2Ml^\pm \geq m\omega \Rightarrow l^\pm \geq \frac{m}{2M}\omega.$$

Thus,

$$\max\{l^+, l^-\} = \omega - \min\{l^+, l^-\} \leq \left(1 - \frac{m}{2M}\right)\omega.$$

For a fixed splitting depth L , j -th coordinate is partitioned at least $c_s L/d$ times. Thus

$$\text{diam}(\mathcal{B}_L) \leq \sqrt{d} \max_j |I_j| \leq \sqrt{d} \rho^{c_s L/d} \max_j |U_{0,j} - L_{0,j}| \leq \sqrt{d} \text{diam}(\mathcal{M}) \rho^{c_s L/d}.$$

■

B. Proof of Lemma 5

Proof of Lemma 5: The piecewise function $H_{\mu,L}(t)$ is L^2 function, thus $H_{\mu,L}(t) \in L^2([0,1], \mathbb{R}^d)$. For any $m > L$, $\|H_{\mu,m}(t) - H_{\mu,L}(t)\|_\infty \leq \sup \text{diam}(\mathcal{B}_L) \leq C\rho^{c_s L/d}$. As $L \rightarrow \infty$, the left tend to zero. Thus $H_{\mu,L}(t)$ is a Cauchy sequence in a Banach space. Thus, there exists a function $H(t)$ as the limit of $H_{\mu,L}(t)$. Let $H_\mu(t) = H(t)$ we complete the proof. ■

C. Proof of Theorem 7

Proof of Theorem 7: Let

$$\nu := (\mathbf{Q}_\mu)_\# \text{Unif}[0,1], \quad \text{i.e., } \nu(B) = \Pr(\mathbf{Q}_\mu(U) \in B), \quad U \sim \text{Unif}[0,1],$$

for every Borel set $B \subset \mathbb{R}^d$. We prove $\nu = \mu$.

Step 1: Depth- L interval and cell partitions. For each $L \geq 1$, the Hilbert addressing rule (Appendix A) induces a partition of $[0,1]$ into 2^L half-open intervals $\{\mathcal{I}_L(\sigma) : \sigma \in \{0,1\}^L\}$, each satisfying

$$\text{Leb}(\mathcal{I}_L(\sigma)) = 2^{-L}. \tag{16}$$

Let \mathcal{N}_L denote the finite set of endpoints of $\{\mathcal{I}_L(\sigma)\}$, and define $\mathcal{N}_{\text{end}} := \bigcup_{L \geq 1} \mathcal{N}_L$. Then $\text{Leb}(\mathcal{N}_{\text{end}}) = 0$, hence

$$\Pr(U \in \mathcal{N}_{\text{end}}) = 0. \tag{17}$$

For $t \in [0,1] \setminus \mathcal{N}_{\text{end}}$, let $\sigma_L(t) \in \{0,1\}^L$ be the unique address satisfying $t \in \mathcal{I}_L(\sigma_L(t))$, and let $\mathcal{B}_L(t)$ be the corresponding depth- L path cell produced by the HiMAP recursion. For each $\sigma \in \{0,1\}^L$, define the depth- L cell (well-defined outside \mathcal{N}_{end})

$$\mathcal{B}_L(\sigma) := \mathcal{B}_L(t) \quad \text{for any } t \in \mathcal{I}_L(\sigma) \setminus \mathcal{N}_{\text{end}}. \tag{18}$$

By the equiprobable split property (3) applied recursively,

$$\mu(\mathcal{B}_L(\sigma)) = 2^{-L}, \quad \forall \sigma \in \{0,1\}^L. \tag{19}$$

Step 2: ν and μ coincide on every depth- L cell. Fix $L \geq 1$ and $\sigma \in \{0, 1\}^L$. Let $U \sim \text{Unif}[0, 1]$ and work on the event $\{U \notin \mathcal{N}_{\text{end}}\}$ (which has probability one by (17)). Then $\sigma_L(U)$ is well-defined and $U \in \mathcal{I}_L(\sigma_L(U))$. By construction of the path cells, for any $m \geq L$ we have the nesting

$$\mathcal{B}_m(U) \subset \mathcal{B}_L(U) = \mathcal{B}_L(\sigma_L(U)). \quad (20)$$

Moreover, by definition of the finite-depth map, $\mathbf{H}_{\mu, m}(U) \in \mathcal{B}_m(U)$ for all m . Since each $\mathcal{B}_L(\sigma)$ is an axis-aligned box (hence closed under your interval convention) and $\mathbf{Q}_\mu(U) = \lim_{m \rightarrow \infty} \mathbf{H}_{\mu, m}(U)$ by (5), letting $m \rightarrow \infty$ in (20) yields

$$\mathbf{Q}_\mu(U) \in \mathcal{B}_L(\sigma_L(U)) \quad \text{a.s.} \quad (21)$$

Therefore,

$$\begin{aligned} \nu(\mathcal{B}_L(\sigma)) &= \Pr(\mathbf{Q}_\mu(U) \in \mathcal{B}_L(\sigma)) \geq \Pr(\sigma_L(U) = \sigma) \\ &= \Pr(U \in \mathcal{I}_L(\sigma)) = \text{Leb}(\mathcal{I}_L(\sigma)) = 2^{-L}, \end{aligned} \quad (22)$$

where we used (16) in the last step.

On the other hand, the family $\{\mathcal{B}_L(\sigma) : \sigma \in \{0, 1\}^L\}$ is a partition of $\mathcal{B}_0 = \mathcal{M} \cap \mathcal{S}$ (up to boundary ties of μ -measure zero under Assumption 3(i)), hence

$$1 = \nu(\mathcal{B}_0) = \sum_{\sigma \in \{0, 1\}^L} \nu(\mathcal{B}_L(\sigma)) \geq \sum_{\sigma \in \{0, 1\}^L} 2^{-L} = 1,$$

which forces equality in (22) for every σ :

$$\nu(\mathcal{B}_L(\sigma)) = 2^{-L} = \mu(\mathcal{B}_L(\sigma)), \quad \forall \sigma \in \{0, 1\}^L. \quad (23)$$

Step 3: Extension from cells to all Borel sets. Let

$$\mathcal{C} := \bigcup_{L \geq 1} \{\mathcal{B}_L(\sigma) : \sigma \in \{0, 1\}^L\}.$$

Then \mathcal{C} is a π -system: the intersection of two cells is either empty or one of the finer cells (since the partitions are nested). Define

$$\mathcal{D} := \{B \in \mathcal{B}(\mathbb{R}^d) : \nu(B) = \mu(B)\}.$$

It is standard that \mathcal{D} is a λ -system (closed under complements and disjoint countable unions). By (23), we have $\mathcal{C} \subset \mathcal{D}$.

It remains to note that $\sigma(\mathcal{C})$ contains the Borel σ -field on $\mathcal{B}_0 = \mathcal{M} \cap \mathcal{S}$. Indeed, since $\text{diam}(\mathcal{B}_L(t)) \rightarrow 0$ uniformly in t by Lemma 4, for any open ball $B(\mathbf{x}, \varepsilon)$ we can write

$$B(\mathbf{x}, \varepsilon) \cap \mathcal{B}_0 = \bigcup_{L=1}^{\infty} \bigcup_{\sigma: \mathcal{B}_L(\sigma) \subset B(\mathbf{x}, \varepsilon)} \mathcal{B}_L(\sigma),$$

because for any $\mathbf{y} \in B(\mathbf{x}, \varepsilon) \cap \mathcal{B}_0$, letting $\delta := \varepsilon - \|\mathbf{y} - \mathbf{x}\| > 0$, for L large enough the depth- L cell containing \mathbf{y} has diameter $< \delta$ and hence is contained in $B(\mathbf{x}, \varepsilon)$. The RHS is a countable union of elements of \mathcal{C} , so every open set in \mathcal{B}_0 belongs to $\sigma(\mathcal{C})$, and thus $\mathcal{B}(\mathcal{B}_0) \subset \sigma(\mathcal{C})$.

By the π - λ theorem, $\sigma(\mathcal{C}) \subset \mathcal{D}$, hence $\nu(B) = \mu(B)$ for all Borel $B \subset \mathcal{B}_0$. Since both ν and μ are supported on \mathcal{B}_0 , this implies $\nu = \mu$ on $\mathcal{B}(\mathbb{R}^d)$, i.e.,

$$(\mathbf{Q}_\mu)_\# \text{Unif}[0, 1] = \mu.$$

Identifiability. If $\mathbf{Q}_\mu(t) = \mathbf{Q}_\nu(t)$ for a.e. t , then $(\mathbf{Q}_\mu)_\# \text{Unif}[0, 1] = (\mathbf{Q}_\nu)_\# \text{Unif}[0, 1]$. By the pushforward identity just proved, this gives $\mu = \nu$. This establishes identifiability up to a null set in t . \blacksquare

D. Proof of Proposition 8

Proof of Proposition 8:

(i) Coordinate-wise affine equivariance. Let $T(\mathbf{u}) = \mathbf{A}\mathbf{u} + \mathbf{b}$ with diagonal $\mathbf{A} = \text{diag}(A_1, \dots, A_d) \succ 0$ and $\mathbf{b} \in \mathbb{R}^d$, and set $\tilde{\mu} := T_\# \mu$. For any box $\mathcal{B}_{l-1} = \prod_{r=1}^d [L_{l-1, r}, U_{l-1, r}]$, write $\tilde{\mathcal{B}}_{l-1} := T(\mathcal{B}_{l-1})$. Fix a depth $l \geq 1$ and put $j := j_l = s(l)$. For any $x \in \mathbb{R}$,

$$\tilde{\mu}(\{\mathbf{v} \in \tilde{\mathcal{B}}_{l-1} : v_j \leq x\}) = \mu(\{\mathbf{u} \in \mathcal{B}_{l-1} : (\mathbf{A}\mathbf{u} + \mathbf{b})_j \leq x\}) = \mu\left(\left\{\mathbf{u} \in \mathcal{B}_{l-1} : u_j \leq \frac{x - b_j}{A_j}\right\}\right).$$

Therefore, by the definition in (2) and the monotonicity of $x \mapsto (x - b_j)/A_j$ (since $A_j > 0$), we obtain the median-cut transform

$$q_l(\tilde{\mu}; \tilde{\mathcal{B}}_{l-1}) = A_j q_l(\mu; \mathcal{B}_{l-1}) + b_j. \quad (24)$$

By Assumption 3(ii), the conditional median cut is unique, hence (24) specifies the split location without ambiguity.

We next show that the path cells transform equivariantly:

$$\tilde{\mathcal{B}}_l(t) = T(\mathcal{B}_l(t)) \quad \text{for all } l \geq 0 \text{ and all } t \text{ with a unique expansion.} \quad (25)$$

The claim holds for $l = 0$ since $\tilde{\mathcal{B}}_0(t) = T(\mathcal{B}_0(t))$ by definition. Assume it holds for $l - 1$. Then $\tilde{\mathcal{B}}_{l-1}(t) = T(\mathcal{B}_{l-1}(t))$ is a box, and $\mathcal{B}_l(t)$ is obtained from $\mathcal{B}_{l-1}(t)$ by splitting the j -th coordinate interval at $q_l(\mu; \mathcal{B}_{l-1}(t))$ and selecting the child indicated by the address bit $\sigma_l(t)$; similarly, $\tilde{\mathcal{B}}_l(t)$ is obtained from $\tilde{\mathcal{B}}_{l-1}(t)$ by splitting at $q_l(\tilde{\mu}; \tilde{\mathcal{B}}_{l-1}(t))$ and selecting the same address bit. Applying (24) with $\mathcal{B}_{l-1} = \tilde{\mathcal{B}}_{l-1}(t)$ yields

$$q_l(\tilde{\mu}; \tilde{\mathcal{B}}_{l-1}(t)) = A_j q_l(\mu; \mathcal{B}_{l-1}(t)) + b_j,$$

which implies that the two children of $\tilde{\mathcal{B}}_{l-1}(t)$ are exactly the images under T of the two children of $\mathcal{B}_{l-1}(t)$. Hence $\tilde{\mathcal{B}}_l(t) = T(\mathcal{B}_l(t))$, proving (25) by induction.

Now fix any coordinate $r \in \{1, \dots, d\}$ and depth $L \geq 1$, and recall $k_r(L) := \max\{l \leq L : s(l) = r\}$. Applying (24) at level $l = k_r(L)$ gives, for all t with a unique expansion,

$$q_{k_r(L)}(\tilde{\mu}; \tilde{\mathcal{B}}_{k_r(L)-1}(t)) = A_r q_{k_r(L)}(\mu; \mathcal{B}_{k_r(L)-1}(t)) + b_r.$$

Therefore,

$$\mathbf{H}_{\tilde{\mu}, L}(t) = \mathbf{A} \mathbf{H}_{\mu, L}(t) + \mathbf{b}.$$

Letting $L \rightarrow \infty$ and using $\mathbf{Q}_\mu(t) = \lim_{L \rightarrow \infty} \mathbf{H}_{\mu, L}(t)$ yields $\mathbf{Q}_{\tilde{\mu}}(t) = \mathbf{A} \mathbf{Q}_\mu(t) + \mathbf{b}$ for a.e. t , proving (i).

(ii) L^r Embedding. For $r \geq 1$, recall the definition

$$d_{\text{HiMAP}, r}(\mu, \nu) := \left(\int_0^1 \|\mathbf{Q}_\mu(t) - \mathbf{Q}_\nu(t)\|^r dt \right)^{1/r}, \quad d_{\text{HiMAP}, r}^r(\mu, \nu) = \int_0^1 \|\mathbf{Q}_\mu(t) - \mathbf{Q}_\nu(t)\|^r dt.$$

Metric properties. Nonnegativity and symmetry are immediate. If $\mu = \nu$, then $\mathbf{Q}_\mu = \mathbf{Q}_\nu$ a.e., hence $d_{\text{HiMAP}, r}(\mu, \nu) = 0$. Conversely, if $d_{\text{HiMAP}, r}(\mu, \nu) = 0$, then $\mathbf{Q}_\mu(t) = \mathbf{Q}_\nu(t)$ for a.e. t , and identifiability from Theorem 7 yields $\mu = \nu$. For the triangle inequality, for any $\mu, \nu, \tau \in \mathcal{P}_\infty(\mathbb{R}^d)$,

$$\begin{aligned} d_{\text{HiMAP}, r}(\mu, \nu) &= \left(\int_0^1 \|\mathbf{Q}_\mu(t) - \mathbf{Q}_\nu(t)\|^r dt \right)^{1/r} \\ &= \left(\int_0^1 \|(\mathbf{Q}_\mu(t) - \mathbf{Q}_\tau(t)) + (\mathbf{Q}_\tau(t) - \mathbf{Q}_\nu(t))\|^r dt \right)^{1/r} \\ &\leq \left(\int_0^1 \|\mathbf{Q}_\mu(t) - \mathbf{Q}_\tau(t)\|^r dt \right)^{1/r} + \left(\int_0^1 \|\mathbf{Q}_\tau(t) - \mathbf{Q}_\nu(t)\|^r dt \right)^{1/r} \\ &= d_{\text{HiMAP}, r}(\mu, \tau) + d_{\text{HiMAP}, r}(\tau, \nu), \end{aligned}$$

where the inequality is Minkowski. Hence $d_{\text{HiMAP}, r}$ is a well-defined metric on $\mathcal{P}_\infty(\mathbb{R}^d)$.

Comparison to Wasserstein distance. Let $U \sim \text{Unif}[0, 1]$ and define

$$X := \mathbf{Q}_\mu(U), \quad Y := \mathbf{Q}_\nu(U).$$

By Theorem 7, $X \sim \mu$ and $Y \sim \nu$, hence the joint law $\gamma := \mathcal{L}(X, Y)$ belongs to $\Pi(\mu, \nu)$. Therefore, by the definition of W_r ,

$$\begin{aligned} W_r^r(\mu, \nu) &= \inf_{\pi \in \Pi(\mu, \nu)} \int_{\mathbb{R}^d \times \mathbb{R}^d} \|\mathbf{x} - \mathbf{y}\|^r d\pi(\mathbf{x}, \mathbf{y}) \leq \int_{\mathbb{R}^d \times \mathbb{R}^d} \|\mathbf{x} - \mathbf{y}\|^r d\gamma(\mathbf{x}, \mathbf{y}) \\ &= \mathbb{E}\|X - Y\|^r = \mathbb{E}\|\mathbf{Q}_\mu(U) - \mathbf{Q}_\nu(U)\|^r = \int_0^1 \|\mathbf{Q}_\mu(t) - \mathbf{Q}_\nu(t)\|^r dt = d_{\text{HiMAP}, r}^r(\mu, \nu). \end{aligned}$$

Taking r -th roots yields $W_r(\mu, \nu) \leq d_{\text{HiMAP}, r}(\mu, \nu)$.

(iii) Linear closure. Let $\{\mu_i\}_{i=1}^q \subset \mathcal{P}_\infty(\mathbb{R}^d)$ satisfy Assumption 3, and let weights $\{\lambda_i\}_{i=1}^q \subset \mathbb{R}$ satisfy $\sum_{i=1}^q \lambda_i = 1$ (affine weights are allowed). Define the candidate map

$$\mathbf{Q}_\oplus(t) := \sum_{i=1}^q \lambda_i \mathbf{Q}_{\mu_i}(t), \quad t \in [0, 1]. \quad (26)$$

We will construct a probability measure $\mu_\oplus \in \mathcal{P}_\infty(\mathbb{R}^d)$ such that $\mathbf{Q}_{\mu_\oplus}(t) = \mathbf{Q}_\oplus(t)$ for a.e. t .

Step 1: Define a consistent tree of combined boxes. Fix $L \geq 1$ and $\sigma \in \{0, 1\}^L$. For each i , define the depth- L cell

$$\mathcal{B}_L^{(i)}(\sigma) := \mathcal{B}_L^{\mu_i}(t) \quad \text{for any } t \in \mathcal{I}_L(\sigma), \quad (27)$$

which is well-defined for all σ (outside a null set of interval endpoints). Each $\mathcal{B}_L^{(i)}(\sigma)$ is an axis-aligned box, and by the equiprobable split property (3) we have

$$\mu_i(\mathcal{B}_L^{(i)}(\sigma)) = 2^{-L}, \quad \forall \sigma \in \{0, 1\}^L. \quad (28)$$

Define the *combined* depth- L box by

$$\mathcal{B}_L^{(\oplus)}(\sigma) := \bigoplus_{i=1}^q \lambda_i \odot \mathcal{B}_L^{(i)}(\sigma). \quad (29)$$

Then $\mathcal{B}_L^{(\oplus)}(\sigma)$ is an axis-aligned box for every σ . Moreover, the family $\{\mathcal{B}_L^{(\oplus)}(\sigma)\}$ is tree-consistent across depths: if $\sigma^- \in \{0, 1\}^{L-1}$ is the parent of σ and $\sigma = \sigma^- b$ with $b \in \{0, 1\}$, then each $\mathcal{B}_L^{(i)}(\sigma)$ is one of the two children of $\mathcal{B}_{L-1}^{(i)}(\sigma^-)$ obtained by splitting the $j_L = s(L)$ -th interval at $q_L(\mu_i; \mathcal{B}_{L-1}^{(i)}(\sigma^-))$. Consequently, by the coordinate-wise form of (12)–(13), $\mathcal{B}_L^{(\oplus)}(\sigma)$ is one of the two children of $\mathcal{B}_{L-1}^{(\oplus)}(\sigma^-)$ obtained by splitting the j_L -th interval at the affine combination

$$q_L^{(\oplus)}(\sigma^-) := \sum_{i=1}^q \lambda_i q_L(\mu_i; \mathcal{B}_{L-1}^{(i)}(\sigma^-)). \quad (30)$$

(In particular, the left/right endpoints of the splitting coordinate also combine affinely, so the resulting two children are exactly the images under $\bigoplus_i \lambda_i \odot (\cdot)$ of the corresponding children of $\mathcal{B}_{L-1}^{(\oplus)}(\sigma^-)$.)

Step 2: Construct μ_{\oplus} via a projective (nested-box) limit. Let $U \sim \text{Unif}[0, 1]$. For each L , set $\sigma := \sigma_L(U)$ and define

$$\mathbf{x}_L := \sum_{i=1}^q \lambda_i \mathbf{H}_{\mu_i, L}(U). \quad (31)$$

For each i , $\mathbf{H}_{\mu_i, L}(U)$ belongs to the depth- L box $\mathcal{B}_L^{(i)}(\sigma_L(U))$ by construction of $\mathbf{H}_{\mu_i, L}$; hence, by (29),

$$\mathbf{x}_L \in \mathcal{B}_L^{(\oplus)}(\sigma_L(U)) \quad \text{for all } L \geq 1 \text{ a.s.} \quad (32)$$

By tree-consistency, the boxes are nested along the random address: $\mathcal{B}_L^{(\oplus)}(\sigma_L(U)) \subset \mathcal{B}_{L-1}^{(\oplus)}(\sigma_{L-1}(U))$. Assumption 3(iii) (diameter shrinkage for the HiMAP partition) implies that $\text{diam}(\mathcal{B}_L^{(i)}(\sigma)) \rightarrow 0$ as $L \rightarrow \infty$, uniformly in σ . Using the bounds $\text{diam}(\lambda \odot R) = |\lambda| \text{diam}(R)$ and $\text{diam}(R \oplus S) \leq \text{diam}(R) + \text{diam}(S)$, we obtain

$$\text{diam}(\mathcal{B}_L^{(\oplus)}(\sigma)) \leq \sum_{i=1}^q |\lambda_i| \text{diam}(\mathcal{B}_L^{(i)}(\sigma)) \xrightarrow{L \rightarrow \infty} 0,$$

uniformly in σ . Therefore, the nested boxes $\mathcal{B}_L^{(\oplus)}(\sigma_L(U))$ shrink to a single point, and $\{\mathbf{x}_L\}_{L \geq 1}$ is a Cauchy sequence in \mathbb{R}^d a.s. Let $\mathbf{x}_{\infty} := \lim_{L \rightarrow \infty} \mathbf{x}_L$.

Define

$$\mu_{\oplus} := (\mathbf{x}_{\infty})_{\#} \text{Unif}[0, 1]. \quad (33)$$

Since the boxes $\mathcal{B}_L^{(\oplus)}(\sigma)$ are all contained in the bounded initial box $\mathcal{B}_0(t) = \mathcal{M} \cap \mathcal{S}$ combined affinely, μ_{\oplus} has bounded support and thus belongs to $\mathcal{P}_{\infty}(\mathbb{R}^d)$.

Step 3: Identify $\mathbf{H}_{\mu_{\oplus}, L}$ and $\mathbf{Q}_{\mu_{\oplus}}$. Fix $L \geq 1$ and $\sigma \in \{0, 1\}^L$. Using (33) and the definition of \mathbf{x}_{∞} as a limit along the random address,

$$\mu_{\oplus}(\mathcal{B}_L^{(\oplus)}(\sigma)) = \mathbb{P}(\sigma_L(U) = \sigma) = \text{Leb}(\mathcal{I}_L(\sigma)) = 2^{-L}.$$

Hence each depth- L box $\mathcal{B}_L^{(\oplus)}(\sigma)$ has mass 2^{-L} , and for every parent $\sigma^- \in \{0, 1\}^{L-1}$, each of its two children has mass $2^{-L} = \frac{1}{2} 2^{-(L-1)}$. Therefore, the splitting location $q_L^{(\oplus)}(\sigma^-)$ in (30) is a valid conditional median cut for μ_{\oplus} on the parent box $\mathcal{B}_{L-1}^{(\oplus)}(\sigma^-)$ in the sense of (2). By uniqueness (Assumption 3(ii)), the HiMAP recursion for μ_{\oplus} must follow the same tree of boxes $\{\mathcal{B}_L^{(\oplus)}(\sigma)\}$ and use the same cut points (30).

Consequently, for every L and every t with a unique expansion,

$$\mathbf{H}_{\mu_{\oplus}, L}(t) = \sum_{i=1}^q \lambda_i \mathbf{H}_{\mu_i, L}(t). \quad (34)$$

Letting $L \rightarrow \infty$ and using the definition $\mathbf{Q}_\mu(t) = \lim_{L \rightarrow \infty} \mathbf{H}_{\mu,L}(t)$ gives, for a.e. t ,

$$\mathbf{Q}_{\mu_\oplus}(t) = \lim_{L \rightarrow \infty} \mathbf{H}_{\mu_\oplus,L}(t) = \sum_{i=1}^q \lambda_i \lim_{L \rightarrow \infty} \mathbf{H}_{\mu_i,L}(t) = \sum_{i=1}^q \lambda_i \mathbf{Q}_{\mu_i}(t) = \mathbf{Q}_\oplus(t),$$

which proves (iii). ■

Remark 14 (connection to the barycenter variational argument). *In the Hilbert space $L^2([0, 1]; \mathbb{R}^d)$, the unconstrained minimizer of $h \mapsto \sum_{i=1}^q \lambda_i \int_0^1 \|\mathbf{Q}_{\mu_i}(t) - h(t)\|_2^2 dt$ is $h^*(t) = \sum_{i=1}^q \lambda_i \mathbf{Q}_{\mu_i}(t)$. Part (iii) shows this h^* is feasible, i.e. equals \mathbf{Q}_{μ_\oplus} for some μ_\oplus , which is the key mechanism enabling affine-weight barycenters and Fréchet regression in our HiMAP geometry.*

E. Proof of Theorem 9

Before proving Thm 9, we give the following auxiliary lemma.

Lemma 15 (Empirical-process increment bound for Ξ_2). *Let*

$$\Delta\left(q^{(L)} + h^{(L)}, q^{(L)}\right) := \Psi_{(L)}(\cdot; q^{(L)} + h^{(L)}) - \Psi_{(L)}(\cdot; q^{(L)}),$$

where $q^{(L)} = q^{(L)}(t)$ is the population cut vector at depth L along the fixed t -path. Then for any $\eta > 0$,

$$\sup_{\|S_L^{-1} h^{(L)}\|_2 \leq \eta} \left\| (P_n - P) \Delta\left(q^{(L)} + h^{(L)}, q^{(L)}\right) \right\|_2 \lesssim O_p\left(n^{-1/2} \eta^{1/2}\right).$$

Moreover, if $\|S_L^{-1} h_n^{(L)}\|_2 = o_p(1)$, then

$$\left\| (P_n - P) \Delta\left(q^{(L)} + h_n^{(L)}, q^{(L)}\right) \right\|_2 = o_p(n^{-1/2}).$$

Proof of Lemma 15: For $1 \leq l \leq L$, denote the l -th coordinate of Δ by

$$\Delta_l\left(q^{(L)} + h^{(L)}, q^{(L)}\right)(\mathbf{u}) := \Psi_l(\mathbf{u}; q^{(L)} + h^{(L)}) - \Psi_l(\mathbf{u}; q^{(L)}).$$

We first bound the $L^1(P)$ size of Δ_l in terms of $h^{(l)}$.

Step 1: a pointwise decomposition. Using (14), write

$$\begin{aligned} \Delta_l &= \left(\mathbf{1}\{\mathbf{u} \in \mathcal{B}_{l-1}(q^{(l-1)} + h^{(l-1)})\} - \mathbf{1}\{\mathbf{u} \in \mathcal{B}_{l-1}(q^{(l-1)})\} \right) \left(\mathbf{1}\{u_{j_l} \leq q_l + h_l\} - \frac{1}{2} \right) \\ &\quad + \mathbf{1}\{\mathbf{u} \in \mathcal{B}_{l-1}(q^{(l-1)})\} \left(\mathbf{1}\{u_{j_l} \leq q_l + h_l\} - \mathbf{1}\{u_{j_l} \leq q_l\} \right). \end{aligned}$$

Hence, by $|\mathbf{1}\{u_{j_l} \leq q_l + h_l\} - \frac{1}{2}| \leq 1$ and triangle inequality,

$$|\Delta_l| \leq A_l + B_l, \tag{35}$$

where

$$\begin{aligned} A_l &:= \mathbf{1}\{\mathbf{u} \in \mathcal{B}_{l-1}(q^{(l-1)})\} |\mathbf{1}\{u_{j_l} \leq q_l + h_l\} - \mathbf{1}\{u_{j_l} \leq q_l\}|, \\ B_l &:= \left| \mathbf{1}\{\mathbf{u} \in \mathcal{B}_{l-1}(q^{(l-1)} + h^{(l-1)})\} - \mathbf{1}\{\mathbf{u} \in \mathcal{B}_{l-1}(q^{(l-1)})\} \right|. \end{aligned}$$

Step 2: bound $P(A_l)$. Note that $A_l(\mathbf{U}) = 1$ implies simultaneously $\mathbf{U} \in \mathcal{B}_{l-1}(q^{(l-1)})$ and U_{j_l} lies between q_l and $q_l + h_l$ (in either direction). Therefore,

$$P(A_l) \leq P\left(\mathbf{U} \in \mathcal{B}_{l-1}(q^{(l-1)}), U_{j_l} \in [q_l, q_l + h_l]\right).$$

Conditioning on $\mathbf{U} \in \mathcal{B}_{l-1}(q^{(l-1)})$ and using $\mu(\mathcal{B}_{l-1}) = 2^{-(l-1)}$,

$$\begin{aligned} P(A_l) &= \mu(\mathcal{B}_{l-1}) \cdot P\left(U_{j_l} \in [q_l, q_l + h_l] \mid \mathbf{U} \in \mathcal{B}_{l-1}\right) \\ &\leq 2^{-(l-1)} \cdot \sup_{x \in I_{l-1, j_l}(t)} f_{U_{j_l} | \mathbf{U} \in \mathcal{B}_{l-1}}(x) \cdot |h_l|. \end{aligned}$$

By the density bounds $m \leq f \leq M$ on $\mathcal{B}_{l-1} = \prod_r I_{l-1, r}(t)$, the conditional density satisfies the uniform bound

$$f_{U_{j_l} | \mathbf{U} \in \mathcal{B}_{l-1}}(x) = \frac{\int_{\prod_{r \neq j_l} I_{l-1, r}(t)} f(x, \mathbf{u}_{-j_l}) d\mathbf{u}_{-j_l}}{\int_{I_{l-1, j_l}(t)} \int_{\prod_{r \neq j_l} I_{l-1, r}(t)} f(x', \mathbf{u}_{-j_l}) d\mathbf{u}_{-j_l} dx'} \leq \frac{M}{m} \cdot \frac{1}{|I_{l-1, j_l}(t)|} = \frac{1}{c_- |I_s(t)|}.$$

Thus

$$P(A_l) \leq \frac{2^{-(l-1)}}{c_-} \frac{|h_l|}{|I_{s(l)}|}. \quad (36)$$

Step 3: bound $P(B_l)$. The event $B_l(\mathbf{U}) = 1$ means \mathbf{U} lies in the symmetric difference of two depth- $(l-1)$ boxes whose boundaries differ only through the earlier perturbations h^1, \dots, h^{l-1} . Since \mathcal{B}_{l-1} is an axis-aligned box, changing a single earlier cut q_r (for $r < l$) affects membership only through a ‘‘slab’’ of thickness $|h_r|$ along the coordinate $j_r = s(r)$, inside the then-current cell. Consequently,

$$B_l(\mathbf{U}) \leq \sum_{r=1}^{l-1} \mathbf{1}\left\{ \mathbf{U} \in \mathcal{B}_{r-1}(q^{(r-1)}), U_{j_r} \in [q_r, q_r + h_r] \right\}.$$

Taking expectations and repeating the conditional-density bound used for (36) yields

$$P(B_l) \leq \sum_{r=1}^{l-1} \frac{2^{-(r-1)}}{c_-} \frac{|h_r|}{|I_{s(r)}|} \leq \frac{1}{c_-} \sum_{r=1}^{l-1} 2^{-(l-1)} \frac{|h_r|}{|I_{s(r)}|}, \quad (37)$$

where in the last inequality we used $\mu(\mathcal{B}_{l-1}) = 2^{-(l-1)}$ and the fact that the relevant slabs are further restricted by the path constraints down to depth $l-1$, contributing the factor $2^{-(l-1)}$ (up to constants; the proof only needs a uniform geometric factor proportional to $\mu(\mathcal{B}_{l-1})$).

Step 4: combine to control $P|\Delta_l|$ and its empirical fluctuations. From (35), (36), and (37),

$$P|\Delta_l| \lesssim \sum_{r=1}^l 2^{-(l-1)} \frac{|h_r|}{|I_{s(r)}|}. \quad (38)$$

Also, $|\Delta_l| \leq 1$.

Define the function class

$$\mathcal{F}_{l,\eta} := \left\{ \Delta_l(q^{(L)} + h^{(L)}, q^{(L)}) : \|S_L^{-1}h^{(L)}\|_2 \leq \eta \right\}.$$

Each Δ_l is a finite linear combination of indicator functions of half-spaces intersected with axis-aligned boxes in \mathbb{R}^d , hence $\mathcal{F}_{l,\eta}$ is a VC-subgraph class with envelope 1. A standard maximal inequality for VC-subgraph classes (e.g. Theorem 2.14.1 of van der Vaart–Wellner [34]) gives

$$\mathbb{E} \sup_{\|S_L^{-1}h^{(L)}\|_2 \leq \eta} |(P_n - P)\Delta_l| \lesssim n^{-1/2} \sup_{\|S_L^{-1}h^{(L)}\|_2 \leq \eta} (P|\Delta_l|)^{1/2}.$$

Using (38) and Cauchy–Schwarz,

$$\sum_{r=1}^l \frac{|h_r|}{|I_{s(r)}|} \leq \left(\sum_{r=1}^l 1^2 \right)^{1/2} \left(\sum_{r=1}^l \left(\frac{|h_r|}{|I_{s(r)}|} \right)^2 \right)^{1/2} \leq l^{1/2} \|S_L^{-1}h^{(L)}\|_2 \leq L^{1/2}\eta.$$

Therefore,

$$\mathbb{E} \sup_{\|S_L^{-1}h^{(L)}\|_2 \leq \eta} |(P_n - P)\Delta_l| \lesssim n^{-1/2} (2^{-(l-1)}\eta)^{1/2}.$$

Finally, by Minkowski and summing over $l = 1, \dots, L$,

$$\begin{aligned} \mathbb{E} \sup_{\|S_L^{-1}h^{(L)}\|_2 \leq \eta} \|(P_n - P)\Delta\|_2 &= \mathbb{E} \sup_{\|S_L^{-1}h^{(L)}\|_2 \leq \eta} \left(\sum_{l=1}^L |(P_n - P)\Delta_l|^2 \right)^{1/2} \\ &\leq \left(\sum_{l=1}^L \left(\mathbb{E} \sup_{\|S_L^{-1}h^{(L)}\|_2 \leq \eta} |(P_n - P)\Delta_l|^2 \right) \right)^{1/2} \\ &\lesssim \left(\sum_{l=1}^L n^{-1} 2^{-(l-1)} \eta \right)^{1/2} \lesssim n^{-1/2} \eta^{1/2}. \end{aligned}$$

This yields the first claim.

For the second claim, take any deterministic sequence $\eta_n \downarrow 0$. Then

$$\begin{aligned} P\left(\left\| (P_n - P)\Delta(q^{(L)} + h_n^{(L)}, q^{(L)}) \right\|_2 > Mn^{-1/2}\eta_n^{1/2} \right) \\ \leq P(\|S_L^{-1}h_n^{(L)}\|_2 > \eta_n) + P\left(\sup_{\|S_L^{-1}h^{(L)}\|_2 \leq \eta_n} \|(P_n - P)\Delta\|_2 > Mn^{-1/2}\eta_n^{1/2} \right). \end{aligned}$$

Since $\|S_L^{-1}h_n^{(L)}\|_2 = o_p(1)$, the first term $\rightarrow 0$ for any $\eta_n \downarrow 0$. The first part of the lemma implies the second term $\rightarrow 0$ as $n \rightarrow \infty$ and then $M \rightarrow \infty$. Hence $\|(P_n - P)\Delta(q^{(L)} + h_n^{(L)}, q^{(L)})\|_2 = o_p(n^{-1/2})$. ■

We then begin to prove Thm. 9.

Proof of Theorem 9: We prove the stated pointwise rate for fixed t .

Step 0: error decomposition. By the triangle inequality,

$$\left\| \widehat{\mathbf{Q}}_{\mu,L}(t) - \mathbf{Q}_{\mu}(t) \right\|_2 \leq \underbrace{\left\| \widehat{\mathbf{Q}}_{\mu,L}(t) - \mathbf{H}_{\mu,L}(t) \right\|_2}_{\text{statistical error}} + \underbrace{\left\| \mathbf{H}_{\mu,L}(t) - \mathbf{Q}_{\mu}(t) \right\|_2}_{\text{geometric approximation}}. \quad (39)$$

By Lemma 4 and the definition $\mathbf{Q}_{\mu}(t) = \lim_{L \rightarrow \infty} \mathbf{H}_{\mu,L}(t)$,

$$\left\| \mathbf{H}_{\mu,L}(t) - \mathbf{Q}_{\mu}(t) \right\|_2 \leq \text{diam}(\mathcal{B}_L(t)) \lesssim \rho^{c_s L/d}. \quad (40)$$

It remains to bound $\left\| \widehat{\mathbf{Q}}_{\mu,L}(t) - \mathbf{H}_{\mu,L}(t) \right\|_2$.

Step 1: Z-estimation expansion for the cut vector. Let $q^{(L)} := q^{(L)}(t)$ and $q_n^{(L)} := \widehat{q}^{(L)}(t)$, and set $h_n^{(L)} := q_n^{(L)} - q^{(L)}$. By construction,

$$P_n \Psi_{(L)}(\cdot; q_n^{(L)}) = \mathbf{0}, \quad P \Psi_{(L)}(\cdot; q^{(L)}) = \mathbf{0}.$$

Write the Jacobian (lower-triangular) matrix

$$J^{(L)} := \left. \frac{\partial}{\partial q} P \Psi_{(L)}(\cdot; q) \right|_{q=q^{(L)}} \in \mathbb{R}^{L \times L}.$$

A Taylor expansion of $P \Psi_{(L)}(\cdot; q_n^{(L)})$ around $q^{(L)}$ gives

$$P \Psi_{(L)}(\cdot; q_n^{(L)}) = J^{(L)} h_n^{(L)} + r_{n,L}, \quad (41)$$

where the remainder admits the integral representation

$$r_{n,L} = \int_0^1 \left(J^{(L)}(q^{(L)} + \tau h_n^{(L)}) - J^{(L)}(q^{(L)}) \right) h_n^{(L)} d\tau. \quad (42)$$

Next, decompose

$$(P_n - P) \Psi_{(L)}(\cdot; q_n^{(L)}) = (P_n - P) \Psi_{(L)}(\cdot; q^{(L)}) + (P_n - P) \Delta(q^{(L)} + h_n^{(L)}, q^{(L)}),$$

with Δ as in Lemma 15. Using $P_n \Psi_{(L)}(\cdot; q_n^{(L)}) = \mathbf{0}$ and $P \Psi_{(L)}(\cdot; q^{(L)}) = \mathbf{0}$, combine (41) to obtain

$$J^{(L)} h_n^{(L)} = -(P_n - P) \Psi_{(L)}(\cdot; q^{(L)}) - (P_n - P) \Delta(q^{(L)} + h_n^{(L)}, q^{(L)}) - r_{n,L}. \quad (43)$$

Finally, because $\widehat{\mathbf{Q}}_{\mu,L}(t) - \mathbf{H}_{\mu,L}(t) = D^{(L)} h_n^{(L)}$, define

$$R_L := D^{(L)} (J^{(L)})^{-1},$$

and rewrite (43) as

$$\widehat{\mathbf{Q}}_{\mu,L}(t) - \mathbf{H}_{\mu,L}(t) = -R_L \left\{ (P_n - P) \Psi_{(L)}(\cdot; q^{(L)}) + (P_n - P) \Delta(q^{(L)} + h_n^{(L)}, q^{(L)}) + r_{n,L} \right\}. \quad (44)$$

Hence

$$\left\| \widehat{\mathbf{Q}}_{\mu,L}(t) - \mathbf{H}_{\mu,L}(t) \right\|_2 \leq \Xi_1 + \Xi_2 + \Xi_3, \quad (45)$$

where

$$\Xi_1 := \|R_L (P_n - P) \Psi_{(L)}(\cdot; q^{(L)})\|_2, \quad \Xi_2 := \|R_L (P_n - P) \Delta(q^{(L)} + h_n^{(L)}, q^{(L)})\|_2, \quad \Xi_3 := \|R_L r_{n,L}\|_2.$$

Step 2: bound Ξ_1 (baseline empirical process) and $\|R_L\|_{\text{op}}$.

Step 2.1: $\|(P_n - P) \Psi_{(L)}(\cdot; q^{(L)})\|_2 = O_p(n^{-1/2})$. For each $1 \leq l \leq L$,

$$\Psi_l(\mathbf{U}; q^{(l)}) = \mathbf{1}\{\mathbf{U} \in \mathcal{B}_{l-1}(t)\} \left(\mathbf{1}\{U_{j_l} \leq q_l\} - \frac{1}{2} \right),$$

so $|\Psi_l| \leq \frac{1}{2} \mathbf{1}\{\mathbf{U} \in \mathcal{B}_{l-1}(t)\}$ and $\mu(\mathcal{B}_{l-1}(t)) = 2^{-(l-1)}$. Thus

$$\text{Var}(\Psi_l(\mathbf{U}; q^{(l)})) \leq \mathbb{E}[\Psi_l^2] \leq \frac{1}{4} 2^{-(l-1)}.$$

Because $(P_n - P)\Psi_l = n^{-1} \sum_{i=1}^n (\Psi_l(\mathbf{U}_i) - P\Psi_l)$ and the \mathbf{U}_i are i.i.d.,

$$\mathbb{E} |(P_n - P)\Psi_l|^2 = \frac{1}{n} \text{Var}(\Psi_l) \leq \frac{1}{4n} 2^{-(l-1)}.$$

Summing over l ,

$$\mathbb{E} \left\| (P_n - P)\Psi_{(L)}(\cdot; q^{(L)}) \right\|_2^2 = \sum_{l=1}^L \mathbb{E} |(P_n - P)\Psi_l|^2 \leq \frac{1}{4n} \sum_{l=1}^{\infty} 2^{-(l-1)} = O(n^{-1}),$$

so $\|(P_n - P)\Psi_{(L)}(\cdot; q^{(L)})\|_2 = O_p(n^{-1/2})$.

Step 2.2: structure and bounds for $J^{(L)}$ and $(J^{(L)})^{-1}$. The matrix $J^{(L)}$ is lower triangular because Ψ_l depends only on $q^{(l)}$. We first bound its diagonal entries. Differentiating under the integral (using the uniqueness of the conditional median),

$$\begin{aligned} (J^{(L)})_{ll} &= \frac{\partial}{\partial q_l} P\Psi_l(\mathbf{U}; q^{(l)}) = \mu(\mathcal{B}_{l-1}(t)) f_{U_{j_l} | \mathbf{U} \in \mathcal{B}_{l-1}(t)}(q_l) \\ &= 2^{-(l-1)} f_{U_{j_l} | \mathbf{U} \in \mathcal{B}_{l-1}(t)}(q_l). \end{aligned} \quad (46)$$

By the same conditional-density bound used in the lemma proof,

$$f_{U_{j_l} | \mathbf{U} \in \mathcal{B}_{l-1}(t)}(q_l) \in \left[\frac{m}{M} \cdot \frac{1}{|I_s(t)|}, \frac{M}{m} \cdot \frac{1}{|I_s(t)|} \right] = \left[\frac{c_-}{|I_s(t)|}, \frac{1}{c_- |I_s(t)|} \right].$$

Therefore

$$(J^{(L)})_{ll} \in \left[c_- \frac{2^{-(l-1)}}{|I_s(t)|}, \frac{1}{c_-} \frac{2^{-(l-1)}}{|I_s(t)|} \right]. \quad (47)$$

For $j < l$, $J_{lj}^{(L)} = \partial_{q^j} P\Psi_l(q^{(l)})$ arises only through the dependence of $\mathcal{B}_{l-1}(q^{(l-1)})$ on q^j , i.e. boundary contributions. A direct boundary differentiation (Dirac delta on the cutting hyperplane) yields the same scaling as (47):

$$|J_{lj}^{(L)}| \lesssim \frac{2^{-(l-1)}}{|I_s(j)|} \quad (j < l), \quad (48)$$

with constants depending only on (m, M) and the initial aspect ratio.

Step 2.3: normalization and an explicit exponential bound for $\|(J^{(L)})^{-1}\|_{\text{op}}$. Define

$$T_L := \text{diag}(t_1, \dots, t_L), \quad t_l := (2^{l-1} |I_s(t)|)^{1/2}, \quad B^{(L)} := T_L J^{(L)} T_L.$$

Then $J^{(L)} = T_L^{-1} B^{(L)} T_L^{-1}$ and $(J^{(L)})^{-1} = T_L (B^{(L)})^{-1} T_L$.

By (47),

$$B_{ll}^{(L)} = t_l^2 (J^{(L)})_{ll} = 2^{l-1} |I_s(t)| (J^{(L)})_{ll} \in [c_-, 1/c_-].$$

For $j < l$, using (48),

$$|B_{lj}^{(L)}| = t_l |J_{lj}^{(L)}| t_j \lesssim (2^{l-1} |I_s(t)|)^{1/2} \frac{2^{-(l-1)}}{|I_s(j)|} (2^{j-1} |I_s(j)|)^{1/2} \lesssim 2^{-(l-j)/2} \left(\frac{|I_s(t)|}{|I_s(j)|} \right)^{1/2}.$$

Since along a fixed path each $|I_s(\cdot)|$ is always between W_{\min} and W_{\max} ,

$$\left(\frac{|I_s(t)|}{|I_s(j)|} \right)^{1/2} \leq \left(\frac{W_{\max}}{W_{\min}} \right)^{1/2} = C_{\text{ratio}}^{1/2},$$

and hence

$$|B_{lj}^{(L)}| \lesssim C_{\text{ratio}}^{1/2} 2^{-(l-j)/2} \quad (j < l). \quad (49)$$

Write $B^{(L)} = D + N$ where $D = \text{diag}(B_{11}^{(L)}, \dots, B_{LL}^{(L)})$ and N is strictly lower triangular. Then $D^{-1}N$ is strictly lower triangular and nilpotent of index L . Moreover, by (49) and $|D_{ll}| \geq c_-$,

$$|(D^{-1}N)_{lj}| = \frac{|B_{lj}^{(L)}|}{|B_{ll}^{(L)}|} \lesssim \frac{C_{\text{ratio}}^{1/2}}{c_-} 2^{-(l-j)/2}.$$

Consequently,

$$\|D^{-1}N\|_1 = \max_{1 \leq l \leq L} \sum_{j < l} |(D^{-1}N)_{lj}| \lesssim \frac{C_{\text{ratio}}^{1/2}}{c_-} \sum_{k=1}^{\infty} 2^{-k/2} =: \tilde{K}_0 < \infty,$$

and similarly $\|D^{-1}N\|_{\infty} \lesssim \tilde{K}_0$, so $\|D^{-1}N\|_{\text{op}} \leq \sqrt{\|D^{-1}N\|_1 \|D^{-1}N\|_{\infty}} \lesssim \tilde{K}_0$.

Using the finite Neumann series (since $(D^{-1}N)^L = 0$),

$$(B^{(L)})^{-1} = (D(I + D^{-1}N))^{-1} = (I + D^{-1}N)^{-1}D^{-1} = \sum_{k=0}^{L-1} (-D^{-1}N)^k D^{-1}.$$

Therefore

$$\|(B^{(L)})^{-1}\|_{\text{op}} \leq \sum_{k=0}^{L-1} \|D^{-1}N\|_{\text{op}}^k \|D^{-1}\|_{\text{op}} \lesssim \|D^{-1}\|_{\text{op}} \cdot (1 + \tilde{K}_0 + \dots + \tilde{K}_0^{L-1}) \lesssim C_{\text{geom}} K_0^L,$$

for some constants $C_{\text{geom}} > 0$ and $K_0 \geq 1$ independent of L .

Finally,

$$\|(J^{(L)})^{-1}\|_{\text{op}} = \|T_L(B^{(L)})^{-1}T_L\|_{\text{op}} \leq \|T_L\|_{\text{op}}^2 \|(B^{(L)})^{-1}\|_{\text{op}} \lesssim \left(\max_{1 \leq l \leq L} 2^{l-1} |I_{s(l)}| \right) C_{\text{geom}} K_0^L.$$

Using Lemma 4 and the balance condition in Assumption 3(iii), $|I_{s(l)}| \lesssim \rho^{c_s l/d} W_{\text{max}}$, hence $\max_{l \leq L} 2^{l-1} |I_{s(l)}| \lesssim (2\rho^{c_s/d})^L$. Thus there exists $\beta \geq 1$ such that

$$\|(J^{(L)})^{-1}\|_{\text{op}} \lesssim C_J \beta^L, \quad \text{with } \beta := 2\rho^{c_s/d} K_0, \quad (50)$$

and consequently $\|R_L\|_{\text{op}} \leq \|D^{(L)}\|_{\text{op}} \|(J^{(L)})^{-1}\|_{\text{op}} \lesssim C_J \beta^L$.

Putting this together with $\|(P_n - P)\Psi_{(L)}\|_2 = O_p(n^{-1/2})$,

$$\Xi_1 \leq \|R_L\|_{\text{op}} \cdot \|(P_n - P)\Psi_{(L)}(\cdot; q^{(L)})\|_2 = O_p(\beta^L n^{-1/2}). \quad (51)$$

Step 3: bound Ξ_2 using Lemma 15. By Lemma 15,

$$\|(P_n - P)\Delta(q^{(L)} + h_n^{(L)}, q^{(L)})\|_2 = O_p\left(n^{-1/2} \|S_L^{-1} h_n^{(L)}\|_2^{1/2}\right),$$

and if $\|S_L^{-1} h_n^{(L)}\|_2 = o_p(1)$ then it is $o_p(n^{-1/2})$. Using $\Xi_2 \leq \|R_L\|_{\text{op}} \|(P_n - P)\Delta\|_2$ and (50),

$$\Xi_2 = O_p\left(\beta^L n^{-1/2} \|S_L^{-1} h_n^{(L)}\|_2^{1/2}\right). \quad (52)$$

In Step 5 below we verify that $\|S_L^{-1} h_n^{(L)}\|_2 = o_p(1)$ for the choice $L \asymp \log n$, so $\Xi_2 = o_p(\beta^L n^{-1/2})$.

Step 4: bound the Taylor remainder Ξ_3 . From (42),

$$\|r_{n,L}\|_2 \leq \int_0^1 \left\| J^{(L)}(q^{(L)} + \tau h_n^{(L)}) - J^{(L)}(q^{(L)}) \right\|_{\text{op}} \cdot \|h_n^{(L)}\|_2 d\tau.$$

As in the proof of Lemma 15, changing the cut vector by $h_n^{(L)}$ perturbs the box boundaries through slabs of thickness $|h_n^r|$ along coordinate j_r , hence each entry of $\Delta J^{(L)} := J^{(L)}(q^{(L)} + h_n^{(L)}) - J^{(L)}(q^{(L)})$ is bounded (up to constants depending only on m, M) by

$$|\Delta J_{lj}^{(L)}| \lesssim 2^{-(l-1)} \sum_{r=1}^l \frac{|h_n^r|}{|I_{s(r)}|}, \quad j \leq l,$$

which implies, by the same Cauchy-Schwarz argument used in (38),

$$\|\Delta J^{(L)}\|_1 \lesssim \|S_L^{-1} h_n^{(L)}\|_2, \quad \|\Delta J^{(L)}\|_{\infty} \lesssim \|S_L^{-1} h_n^{(L)}\|_2.$$

Therefore,

$$\left\| J^{(L)}(q^{(L)} + \tau h_n^{(L)}) - J^{(L)}(q^{(L)}) \right\|_{\text{op}} \leq \|\Delta J^{(L)}\|_{\text{op}} \leq \sqrt{\|\Delta J^{(L)}\|_1 \|\Delta J^{(L)}\|_{\infty}} \lesssim \|S_L^{-1} h_n^{(L)}\|_2.$$

Moreover, $\|h_n^{(L)}\|_2 \leq \|S_L\|_{\text{op}} \|S_L^{-1} h_n^{(L)}\|_2 \leq W_{\text{max}} \|S_L^{-1} h_n^{(L)}\|_2$. Hence,

$$\|r_{n,L}\|_2 \lesssim W_{\text{max}} \|S_L^{-1} h_n^{(L)}\|_2^2. \quad (53)$$

It follows that

$$\Xi_3 \leq \|R_L\|_{\text{op}} \|r_{n,L}\|_2 \lesssim \beta^L W_{\text{max}} \|S_L^{-1} h_n^{(L)}\|_2^2. \quad (54)$$

Step 5: a self-contained bound for $\|S_L^{-1} h_n^{(L)}\|_2$. Multiply (43) by $S_L^{-1}(J^{(L)})^{-1}$ and take norms:

$$\|S_L^{-1} h_n^{(L)}\|_2 \leq \|S_L^{-1}\|_{\text{op}} \|(J^{(L)})^{-1}\|_{\text{op}} (\|(P_n - P)\Psi_{(L)}\|_2 + \|(P_n - P)\Delta\|_2 + \|r_{n,L}\|_2).$$

Using $\|S_L^{-1}\|_{\text{op}} \leq 1/\min_j |I_{s(j)}| \lesssim MW_{\text{max}}^{d-1} 2^L$, (50), the bound $\|(P_n - P)\Psi_{(L)}\|_2 = O_p(n^{-1/2})$, Lemma 15, and (53), we obtain

$$\|S_L^{-1} h_n^{(L)}\|_2 \lesssim 2^L \beta^L \left(O_p(n^{-1/2}) + O_p\left(n^{-1/2} \|S_L^{-1} h_n^{(L)}\|_2^{1/2}\right) + W_{\text{max}} \|S_L^{-1} h_n^{(L)}\|_2^2 \right).$$

For $L \asymp \log n$ and sufficiently large n , the RHS forces $\|S_L^{-1}h_n^{(L)}\|_2 = o_p(1)$, and in particular yields the leading-order bound

$$\|S_L^{-1}h_n^{(L)}\|_2 = O_p(2^L \beta^L n^{-1/2}). \quad (55)$$

Substituting (55) into (52)–(54) implies

$$\Xi_2 = o_p(2^L \beta^L n^{-1/2}), \quad \Xi_3 = o_p(2^L \beta^L n^{-1/2}).$$

Therefore, by (45) and (51),

$$\left\| \widehat{\mathbf{Q}}_{\mu,L}(t) - \mathbf{H}_{\mu,L}(t) \right\|_2 = O_p(2^L \beta^L n^{-1/2}). \quad (56)$$

Step 6: choose $L = L(n)$ and conclude. Combining (39), (40), and (56),

$$\left\| \widehat{\mathbf{Q}}_{\mu,L}(t) - \mathbf{Q}_{\mu}(t) \right\|_2 \lesssim O_p(2^L \beta^L n^{-1/2}) + \rho^{c_s L/d}.$$

Choosing $L = L(n) \asymp \log n / 2 \log 4K_0$ to balance the two terms yields the stated polynomial rate in n . In particular, with $\gamma = \log_{1/\rho}(4K_0)$ as in Theorem 9, one obtains (after optimizing L) the bound claimed in the theorem statement. ■

APPENDIX D PROOFS FOR SECTION IV

A. Proof of Theorem 11

In the theorem, we use the normalized affine combination (7), so throughout the main argument we assume $\Lambda > 0$. (At the end of the proof, we explain why no minimizer exists when all weights are negative, in which case $\Lambda < 0$.)

Proof of Theorem 11: Step 1: rewrite the Fréchet functional in \mathcal{H} . For any $\nu \in \mathcal{P}_{\infty}(\mathbb{R}^d)$, combining (6) and (15) gives

$$\mathcal{F}(\nu) = \sum_{i=1}^q \lambda_i \|q_i - q_{\nu}\|_{\mathcal{H}}^2. \quad (57)$$

Expanding each squared norm in the Hilbert space,

$$\|q_i - q_{\nu}\|_{\mathcal{H}}^2 = \langle q_i - q_{\nu}, q_i - q_{\nu} \rangle_{\mathcal{H}} = \|q_i\|_{\mathcal{H}}^2 - 2\langle q_i, q_{\nu} \rangle_{\mathcal{H}} + \|q_{\nu}\|_{\mathcal{H}}^2.$$

Plugging this into (57) yields

$$\begin{aligned} \mathcal{F}(\nu) &= \sum_{i=1}^q \lambda_i \|q_i\|_{\mathcal{H}}^2 - 2 \left\langle \sum_{i=1}^q \lambda_i q_i, q_{\nu} \right\rangle_{\mathcal{H}} + \left(\sum_{i=1}^q \lambda_i \right) \|q_{\nu}\|_{\mathcal{H}}^2 \\ &= C_0 - 2\langle g, q_{\nu} \rangle_{\mathcal{H}} + \Lambda \|q_{\nu}\|_{\mathcal{H}}^2, \end{aligned} \quad (58)$$

where $C_0 := \sum_{i=1}^q \lambda_i \|q_i\|_{\mathcal{H}}^2$ does not depend on ν .

Step 2: complete the square and identify the unconstrained minimizer. Since $\Lambda > 0$, we can complete the square in (58):

$$\mathcal{F}(\nu) = C_0 + \Lambda \left\| q_{\nu} - \frac{g}{\Lambda} \right\|_{\mathcal{H}}^2 - \frac{1}{\Lambda} \|g\|_{\mathcal{H}}^2. \quad (59)$$

Therefore, as a functional of $q_{\nu} \in \mathcal{H}$, the unique minimizer is attained at

$$q^* := \frac{g}{\Lambda} = \frac{1}{\Lambda} \sum_{i=1}^q \lambda_i q_i. \quad (60)$$

Step 3: feasibility via Linear Closure (Proposition 8(iii)). Define normalized weights $\alpha_i := \lambda_i / \Lambda$, so that $\sum_{i=1}^q \alpha_i = 1$. Then (60) reads

$$q^* = \sum_{i=1}^q \alpha_i q_i = \sum_{i=1}^q \alpha_i \mathbf{Q}_{\nu_i}.$$

By Proposition 8(iii) (Linear Closure), the affine combination $\sum_{i=1}^q \alpha_i \mathbf{Q}_{\nu_i}$ is itself the HiMAP quantile function of a valid probability measure. Hence there exists $\nu_{\oplus} \in \mathcal{P}_{\infty}(\mathbb{R}^d)$ such that

$$q_{\nu_{\oplus}} = \mathbf{Q}_{\nu_{\oplus}} = q^* = \frac{1}{\Lambda} \sum_{i=1}^q \lambda_i \mathbf{Q}_{\nu_i}, \quad (61)$$

which is exactly (7). In particular, the candidate ν_{\oplus} is feasible for (6).

Step 4: optimality and uniqueness. Let $\nu \in \mathcal{P}_\infty(\mathbb{R}^d)$ be arbitrary. Subtracting (59) evaluated at ν_\oplus from the same expression evaluated at ν , and using (61), we obtain

$$\begin{aligned}\mathcal{F}(\nu) - \mathcal{F}(\nu_\oplus) &= \Lambda \left\| q_\nu - \frac{g}{\Lambda} \right\|_{\mathcal{H}}^2 - \Lambda \left\| q_{\nu_\oplus} - \frac{g}{\Lambda} \right\|_{\mathcal{H}}^2 \\ &= \Lambda \|q_\nu - q_{\nu_\oplus}\|_{\mathcal{H}}^2 \geq 0,\end{aligned}$$

where the last inequality uses $\Lambda > 0$. Hence ν_\oplus is a global minimizer.

Moreover, if $\mathcal{F}(\nu) = \mathcal{F}(\nu_\oplus)$, then $\|q_\nu - q_{\nu_\oplus}\|_{\mathcal{H}}^2 = 0$, i.e. $q_\nu(t) = q_{\nu_\oplus}(t)$ for a.e. t . By Theorem 7, the map $\nu \mapsto \mathbf{Q}_\nu$ is identifiable up to a null set in t , so this implies $\nu = \nu_\oplus$. Therefore, the minimizer is unique. The pushforward representation $\nu_\oplus = (\mathbf{Q}_{\nu_\oplus})_\# \text{Unif}[0, 1]$ follows directly from Theorem 7.

This completes the proof. \blacksquare

Remark 16 (why there is no minimizer when all weights are negative). *If all weights are negative, then $\Lambda = \sum_{i=1}^q \lambda_i < 0$. Fix any $\nu_0 \in \mathcal{P}_\infty(\mathbb{R}^d)$ and consider translations $T_R(\mathbf{u}) = \mathbf{u} + R\mathbf{e}_1$, where $\mathbf{e}_1 = (1, 0, \dots, 0)^\top$ and $R > 0$. Let $\nu_R := (T_R)_\# \nu_0$. By Proposition 8(i) (Affine Equivariance with $\mathbf{A} = \mathbf{I}$ and $\mathbf{b} = R\mathbf{e}_1$),*

$$\mathbf{Q}_{\nu_R}(t) = \mathbf{Q}_{\nu_0}(t) + R\mathbf{e}_1, \quad \text{a.e. } t.$$

Hence, using (15),

$$\begin{aligned}\mathcal{F}(\nu_R) &= \sum_{i=1}^q \lambda_i \int_0^1 \left\| \mathbf{Q}_{\nu_i}(t) - \mathbf{Q}_{\nu_0}(t) - R\mathbf{e}_1 \right\|^2 dt \\ &= \sum_{i=1}^q \lambda_i \left[\int_0^1 \left\| \mathbf{Q}_{\nu_i}(t) - \mathbf{Q}_{\nu_0}(t) \right\|^2 dt - 2R \int_0^1 \mathbf{e}_1^\top (\mathbf{Q}_{\nu_i}(t) - \mathbf{Q}_{\nu_0}(t)) dt + R^2 \|\mathbf{e}_1\|^2 \right] \\ &= C_1 - 2R a_1 + \Lambda R^2,\end{aligned}$$

for constants $C_1 \in \mathbb{R}$ and $a_1 \in \mathbb{R}$ independent of R . Since $\Lambda < 0$, the quadratic term dominates and $\mathcal{F}(\nu_R) \rightarrow -\infty$ as $R \rightarrow \infty$. Therefore $\inf_{\nu \in \mathcal{P}_\infty(\mathbb{R}^d)} \mathcal{F}(\nu) = -\infty$, and no minimizer exists when all weights are negative.

B. Proof of Corollary 13

We next separate predictor-side regularity for *global* and *local* Fréchet regression, and make the dependence on the predictor dimension p explicit.

Assumption 17 (Global Fréchet regression: design and linearity). *Let $\boldsymbol{\mu} := \mathbb{E}(\mathbf{X}) \in \mathbb{R}^p$ and $\boldsymbol{\Sigma} := \text{Var}(\mathbf{X}) \in \mathbb{R}^{p \times p}$. Assume:*

- (G1) (Second moments and conditioning) $\mathbb{E}\|\mathbf{X}\|^4 < \infty$ and $\lambda_{\min}(\boldsymbol{\Sigma}) \geq c_\Sigma > 0$, $\lambda_{\max}(\boldsymbol{\Sigma}) \leq C_\Sigma < \infty$.
(G2) (Sample mean/covariance rates with explicit p) With $\hat{\boldsymbol{\mu}} := m^{-1} \sum_{i=1}^m \mathbf{X}_i$ and $\hat{\boldsymbol{\Sigma}} := m^{-1} \sum_{i=1}^m (\mathbf{X}_i - \hat{\boldsymbol{\mu}})(\mathbf{X}_i - \hat{\boldsymbol{\mu}})^\top$,

$$\|\hat{\boldsymbol{\mu}} - \boldsymbol{\mu}\|_2 = O_p\left(\sqrt{\frac{p}{m}}\right), \quad \|\hat{\boldsymbol{\Sigma}} - \boldsymbol{\Sigma}\|_{\text{op}} = O_p\left(\sqrt{\frac{p}{m}}\right).$$

(For fixed p this is standard under $\mathbb{E}\|\mathbf{X}\|^4 < \infty$; for growing p one may impose a sub-Gaussian design to ensure the same displayed rate.)

- (G3) (Global linearity of the conditional quantile function) *For a.e. $t \in [0, 1]$, the map*

$$\mathbf{g}(\mathbf{x}, t) := \mathbb{E}[\mathbf{Q}_Y(t) \mid \mathbf{X} = \mathbf{x}] \in \mathbb{R}^d$$

is affine in \mathbf{x} : there exist $\mathbf{a}(t) \in \mathbb{R}^d$ and $\mathbf{B}(t) \in \mathbb{R}^{p \times d}$ such that $\mathbf{g}(\mathbf{x}, t) = \mathbf{a}(t) + \mathbf{B}(t)^\top (\mathbf{x} - \boldsymbol{\mu})$. Moreover $\int_0^1 \|\mathbf{a}(t)\|_2^2 dt < \infty$ and $\int_0^1 \|\mathbf{B}(t)\|_F^2 dt < \infty$.

- (G4) (Bounded response map on \mathcal{M}) *There exists $R_{\mathcal{M}} < \infty$ such that if $\text{supp}(Y) \subset \mathcal{M}$, then $\|\mathbf{Q}_Y(t)\|_2 \leq R_{\mathcal{M}}$ for a.e. t .*

Assumption 18 (Local Fréchet regression: design and smoothness). *Fix an interior target point $\mathbf{x} \in \mathbb{R}^p$. Assume:*

- (L1) (Kernel) $K : \mathbb{R}^p \rightarrow \mathbb{R}$ is bounded, symmetric, and compactly supported, $\int K(\mathbf{u}) d\mathbf{u} = 1$, $\int \mathbf{u}K(\mathbf{u}) d\mathbf{u} = \mathbf{0}$, and $\int \mathbf{u}\mathbf{u}^\top K(\mathbf{u}) d\mathbf{u}$ is positive definite. Let $K_h(\mathbf{u}) = h^{-p}K(\mathbf{u}/h)$.

- (L2) (Design density) \mathbf{X} admits a density $f_{\mathbf{X}}$ which is twice continuously differentiable in a neighborhood of \mathbf{x} with $0 < \underline{f} \leq f_{\mathbf{X}}(\mathbf{z}) \leq \bar{f}$ there.

- (L3) (Local moment invertibility) With $\mathbf{v}(\mathbf{z}; \mathbf{x}) := (1, (\mathbf{z} - \mathbf{x})^\top)^\top \in \mathbb{R}^{p+1}$, define

$$\mathbf{S}(\mathbf{x}; h) := \mathbb{E}[K_h(\mathbf{X} - \mathbf{x}) \mathbf{v}(\mathbf{X}; \mathbf{x}) \mathbf{v}(\mathbf{X}; \mathbf{x})^\top].$$

There exists $\underline{\lambda} > 0$ such that for all sufficiently small h , $\lambda_{\min}\{\mathbf{S}(\mathbf{x}; h)\} \geq \underline{\lambda}$.

(L4) (Smooth conditional quantile function) For a.e. t , $\mathbf{g}(\cdot, t)$ is twice continuously differentiable near \mathbf{x} and

$$\int_0^1 \sup_{\mathbf{z} \text{ near } \mathbf{x}} \|\nabla_{\mathbf{z}}^2 \mathbf{g}(\mathbf{z}, t)\|_F^2 dt < \infty.$$

(L5) (Bounded response map on \mathcal{M}) Same as (G4).

(L6) (Bandwidth regime) $h \rightarrow 0$ and $mh^p \rightarrow \infty$ as $m \rightarrow \infty$.

Weights (global and local). For global regression, define the (oracle) weights

$$w_i^{(G)}(\mathbf{x}) := \frac{1}{m} \left\{ 1 + (\mathbf{X}_i - \boldsymbol{\mu})^\top \boldsymbol{\Sigma}^{-1} (\mathbf{x} - \boldsymbol{\mu}) \right\}, \quad i = 1, \dots, m, \quad (62)$$

and the empirical weights (plugging in $\hat{\boldsymbol{\mu}}, \hat{\boldsymbol{\Sigma}}$)

$$\hat{w}_i^{(G)}(\mathbf{x}) := \frac{1}{m} \left\{ 1 + (\mathbf{X}_i - \hat{\boldsymbol{\mu}})^\top \hat{\boldsymbol{\Sigma}}^{-1} (\mathbf{x} - \hat{\boldsymbol{\mu}}) \right\}. \quad (63)$$

For local regression in \mathbb{R}^p , write $\mathbf{e}_1 := (1, 0, \dots, 0)^\top \in \mathbb{R}^{p+1}$ and define the empirical moment matrix

$$\hat{\mathbf{S}}(\mathbf{x}; h) := \frac{1}{m} \sum_{i=1}^m K_h(\mathbf{X}_i - \mathbf{x}) \mathbf{v}(\mathbf{X}_i; \mathbf{x}) \mathbf{v}(\mathbf{X}_i; \mathbf{x})^\top.$$

Define the oracle and empirical local linear weights by

$$w_i^{(L)}(\mathbf{x}; h) := \frac{1}{m} K_h(\mathbf{X}_i - \mathbf{x}) \mathbf{e}_1^\top \mathbf{S}(\mathbf{x}; h)^{-1} \mathbf{v}(\mathbf{X}_i; \mathbf{x}), \quad \hat{w}_i^{(L)}(\mathbf{x}; h) := \frac{1}{m} K_h(\mathbf{X}_i - \mathbf{x}) \mathbf{e}_1^\top \hat{\mathbf{S}}(\mathbf{x}; h)^{-1} \mathbf{v}(\mathbf{X}_i; \mathbf{x}). \quad (64)$$

Lemma 19 (Global weight perturbation (explicit p)). *Under Assumption 17,*

$$\sum_{i=1}^m \left| \hat{w}_i^{(G)}(\mathbf{x}) - w_i^{(G)}(\mathbf{x}) \right| = O_p \left(\sqrt{\frac{p}{m}} \right). \quad (65)$$

Proof of Lemma 19: Let $\Delta_\mu := \hat{\boldsymbol{\mu}} - \boldsymbol{\mu}$ and $\Delta_\Sigma := \hat{\boldsymbol{\Sigma}} - \boldsymbol{\Sigma}$. By (G2), $\|\Delta_\mu\|_2 = O_p(\sqrt{p/m})$ and $\|\Delta_\Sigma\|_{\text{op}} = O_p(\sqrt{p/m})$. Since $\lambda_{\min}(\boldsymbol{\Sigma}) \geq c_\Sigma > 0$ and $\|\Delta_\Sigma\|_{\text{op}} = o_p(1)$, $\hat{\boldsymbol{\Sigma}}$ is invertible w.p. $\rightarrow 1$ and $\|\hat{\boldsymbol{\Sigma}}^{-1}\|_{\text{op}} = O_p(1)$. Using the resolvent identity,

$$\hat{\boldsymbol{\Sigma}}^{-1} - \boldsymbol{\Sigma}^{-1} = \boldsymbol{\Sigma}^{-1} (\boldsymbol{\Sigma} - \hat{\boldsymbol{\Sigma}}) \hat{\boldsymbol{\Sigma}}^{-1},$$

we obtain

$$\|\hat{\boldsymbol{\Sigma}}^{-1} - \boldsymbol{\Sigma}^{-1}\|_{\text{op}} \leq \|\boldsymbol{\Sigma}^{-1}\|_{\text{op}} \|\Delta_\Sigma\|_{\text{op}} \|\hat{\boldsymbol{\Sigma}}^{-1}\|_{\text{op}} = O_p \left(\sqrt{\frac{p}{m}} \right). \quad (66)$$

Now expand (63)–(62):

$$\hat{w}_i^{(G)}(\mathbf{x}) - w_i^{(G)}(\mathbf{x}) = \frac{1}{m} \left[(\mathbf{X}_i - \hat{\boldsymbol{\mu}})^\top \hat{\boldsymbol{\Sigma}}^{-1} (\mathbf{x} - \hat{\boldsymbol{\mu}}) - (\mathbf{X}_i - \boldsymbol{\mu})^\top \boldsymbol{\Sigma}^{-1} (\mathbf{x} - \boldsymbol{\mu}) \right].$$

Add and subtract $(\mathbf{X}_i - \boldsymbol{\mu})^\top \hat{\boldsymbol{\Sigma}}^{-1} (\mathbf{x} - \boldsymbol{\mu})$ and $(\mathbf{X}_i - \boldsymbol{\mu})^\top \boldsymbol{\Sigma}^{-1} (\mathbf{x} - \hat{\boldsymbol{\mu}})$ to obtain the bound

$$\begin{aligned} m \left| \hat{w}_i^{(G)}(\mathbf{x}) - w_i^{(G)}(\mathbf{x}) \right| &\leq \|\mathbf{X}_i - \boldsymbol{\mu}\|_2 \|\hat{\boldsymbol{\Sigma}}^{-1} - \boldsymbol{\Sigma}^{-1}\|_{\text{op}} \|\mathbf{x} - \boldsymbol{\mu}\|_2 \\ &\quad + \|\mathbf{X}_i - \boldsymbol{\mu}\|_2 \|\boldsymbol{\Sigma}^{-1}\|_{\text{op}} \|\Delta_\mu\|_2 + \|\Delta_\mu\|_2 \|\hat{\boldsymbol{\Sigma}}^{-1}\|_{\text{op}} \|\mathbf{x} - \hat{\boldsymbol{\mu}}\|_2. \end{aligned}$$

Summing over i and dividing by m gives

$$\begin{aligned} \sum_{i=1}^m \left| \hat{w}_i^{(G)}(\mathbf{x}) - w_i^{(G)}(\mathbf{x}) \right| &\leq \left(\frac{1}{m} \sum_{i=1}^m \|\mathbf{X}_i - \boldsymbol{\mu}\|_2 \right) \|\hat{\boldsymbol{\Sigma}}^{-1} - \boldsymbol{\Sigma}^{-1}\|_{\text{op}} \|\mathbf{x} - \boldsymbol{\mu}\|_2 \\ &\quad + \left(\frac{1}{m} \sum_{i=1}^m \|\mathbf{X}_i - \boldsymbol{\mu}\|_2 \right) \|\boldsymbol{\Sigma}^{-1}\|_{\text{op}} \|\Delta_\mu\|_2 + \|\Delta_\mu\|_2 \|\hat{\boldsymbol{\Sigma}}^{-1}\|_{\text{op}} \|\mathbf{x} - \hat{\boldsymbol{\mu}}\|_2. \end{aligned}$$

By $\mathbb{E}\|\mathbf{X}\|^4 < \infty$, we have $m^{-1} \sum_{i=1}^m \|\mathbf{X}_i - \boldsymbol{\mu}\|_2 = O_p(1)$, and $\|\mathbf{x} - \hat{\boldsymbol{\mu}}\|_2 = O_p(1)$ for fixed \mathbf{x} . Combining with (G2) and (66) yields (65). \blacksquare

Lemma 20 (Local linear weight perturbation (explicit p)). *Under Assumption 18,*

$$\sum_{i=1}^m \left| \hat{w}_i^{(L)}(\mathbf{x}; h) - w_i^{(L)}(\mathbf{x}; h) \right| = O_p \left(\frac{p}{\sqrt{mh^p}} \right). \quad (67)$$

Proof of Lemma 20: Write $\Delta_S := \widehat{\mathbf{S}}(\mathbf{x}; h) - \mathbf{S}(\mathbf{x}; h)$. Because K is bounded and compactly supported and \mathbf{x} is interior, on the kernel window $\|\mathbf{X}_i - \mathbf{x}\|_2 \leq Ch$, so $\|\mathbf{v}(\mathbf{X}_i; \mathbf{x})\|_2 \leq C_v$. Hence, each entry of the summand $K_h(\mathbf{X}_i - \mathbf{x}) \mathbf{v}(\mathbf{X}_i; \mathbf{x}) \mathbf{v}(\mathbf{X}_i; \mathbf{x})^\top$ is bounded by Ch^{-p} and has variance of order h^{-2p} ; therefore each entry of Δ_S has standard deviation of order $(mh^p)^{-1/2}$. Since $\widehat{\mathbf{S}}$ is $(p+1) \times (p+1)$, a union bound over its entries yields

$$\max_{a,b \in [p+1]} |(\Delta_S)_{ab}| = O_p\left((mh^p)^{-1/2}\right). \quad (68)$$

Consequently,

$$\|\Delta_S\|_{\text{op}} \leq \|\Delta_S\|_F \leq (p+1) \max_{a,b} |(\Delta_S)_{ab}| = O_p\left(\frac{p}{\sqrt{mh^p}}\right). \quad (69)$$

By (L3), $\|\mathbf{S}(\mathbf{x}; h)^{-1}\|_{\text{op}} \leq \underline{\lambda}^{-1}$. Moreover (69) implies $\|\Delta_S\|_{\text{op}} = o_p(1)$, so $\widehat{\mathbf{S}}(\mathbf{x}; h)$ is invertible w.p. $\rightarrow 1$ and $\|\widehat{\mathbf{S}}(\mathbf{x}; h)^{-1}\|_{\text{op}} = O_p(1)$. Using the resolvent identity,

$$\widehat{\mathbf{S}}^{-1} - \mathbf{S}^{-1} = \mathbf{S}^{-1}(\mathbf{S} - \widehat{\mathbf{S}})\widehat{\mathbf{S}}^{-1},$$

we obtain

$$\|\widehat{\mathbf{S}}(\mathbf{x}; h)^{-1} - \mathbf{S}(\mathbf{x}; h)^{-1}\|_{\text{op}} = O_p\left(\frac{p}{\sqrt{mh^p}}\right). \quad (70)$$

Now from (64),

$$\widehat{w}_i^{(L)}(\mathbf{x}; h) - w_i^{(L)}(\mathbf{x}; h) = \frac{1}{m} K_h(\mathbf{X}_i - \mathbf{x}) \mathbf{e}_1^\top \left(\widehat{\mathbf{S}}(\mathbf{x}; h)^{-1} - \mathbf{S}(\mathbf{x}; h)^{-1} \right) \mathbf{v}(\mathbf{X}_i; \mathbf{x}).$$

Hence

$$\sum_{i=1}^m \left| \widehat{w}_i^{(L)}(\mathbf{x}; h) - w_i^{(L)}(\mathbf{x}; h) \right| \leq \|\widehat{\mathbf{S}}(\mathbf{x}; h)^{-1} - \mathbf{S}(\mathbf{x}; h)^{-1}\|_{\text{op}} \cdot \frac{1}{m} \sum_{i=1}^m |K_h(\mathbf{X}_i - \mathbf{x})| \|\mathbf{v}(\mathbf{X}_i; \mathbf{x})\|_2.$$

The second factor is $O_p(1)$ because only $O_p(mh^p)$ terms are nonzero and $|K_h| \lesssim h^{-p}$ on the window:

$$\frac{1}{m} \sum_{i=1}^m |K_h(\mathbf{X}_i - \mathbf{x})| \|\mathbf{v}(\mathbf{X}_i; \mathbf{x})\|_2 = O_p\left(\frac{mh^p}{m} \cdot h^{-p}\right) = O_p(1).$$

Combining with (70) gives (67). \blacksquare

Proof of Corollary 13: Write $\mathbf{g}(\mathbf{x}, t) := \mathbb{E}[\mathbf{Q}_Y(t) \mid \mathbf{X} = \mathbf{x}]$, so that $\mathbf{Q}_{m \oplus(\mathbf{x})}(t) = \mathbf{g}(\mathbf{x}, t)$. Define the oracle (plug-in-free) regression maps

$$\mathbf{Q}_{\widehat{m}^{(G)}(\mathbf{x})}(t) := \sum_{i=1}^m w_i^{(G)}(\mathbf{x}) \mathbf{Q}_{Y_i}(t), \quad \mathbf{Q}_{\widehat{m}^{(L)}(\mathbf{x})}(t) := \sum_{i=1}^m w_i^{(L)}(\mathbf{x}; h) \mathbf{Q}_{Y_i}(t).$$

We treat the global and local cases in parallel by the same decomposition:

$$\begin{aligned} d_{\text{HiMAP},2}(\widehat{m}(\mathbf{x}), m_{\oplus}(\mathbf{x})) &= \left\| \widehat{\mathbf{Q}}_{m(\mathbf{x})} - \mathbf{g}(\mathbf{x}, \cdot) \right\|_{L^2} \\ &\leq \underbrace{\left\| \sum_{i=1}^m \widehat{w}_i(\mathbf{x}) (\widehat{\mathbf{Q}}_{Y_i} - \mathbf{Q}_{Y_i}) \right\|_{L^2}}_{T_1} + \underbrace{\left\| \sum_{i=1}^m (\widehat{w}_i(\mathbf{x}) - w_i(\mathbf{x})) \mathbf{Q}_{Y_i} \right\|_{L^2}}_{T_2} + \underbrace{\left\| \mathbf{Q}_{\widehat{m}(\mathbf{x})} - \mathbf{g}(\mathbf{x}, \cdot) \right\|_{L^2}}_{T_3}, \end{aligned} \quad (71)$$

where (w_i, \widehat{m}) means $(w_i^{(G)}, \widehat{m}^{(G)})$ in the global case and $(w_i^{(L)}, \widehat{m}^{(L)})$ in the local case.

Step 1: quantile estimation term T_1 . Let $\Delta_i := \|\widehat{\mathbf{Q}}_{Y_i} - \mathbf{Q}_{Y_i}\|_{L^2} = d_{\text{HiMAP},2}(\widehat{Y}_i, Y_i)$. By Corollary 10, $\Delta_i = O_p(n^{-c_s/(2d\gamma)})$. For the global case, since $\widehat{w}_i^{(G)}(\mathbf{x}) = m^{-1}\{1 + O_p(1)\}$ and $\mathbb{E}[w^{(G)}(\mathbf{X}, \mathbf{x})^2] < \infty$ under (G1)–(G3),

$$\sum_{i=1}^m (\widehat{w}_i^{(G)}(\mathbf{x}))^2 = \frac{1}{m^2} \sum_{i=1}^m \left(1 + (\mathbf{X}_i - \widehat{\boldsymbol{\mu}})^\top \widehat{\boldsymbol{\Sigma}}^{-1}(\mathbf{x} - \widehat{\boldsymbol{\mu}}) \right)^2 = O_p\left(\frac{1}{m}\right).$$

Then by Cauchy–Schwarz,

$$T_1 \leq \left(\sum_{i=1}^m \widehat{w}_i(\mathbf{x})^2 \right)^{1/2} \left(\sum_{i=1}^m \Delta_i^2 \right)^{1/2} = O_p\left(m^{-1/2}\right) \cdot O_p\left(\sqrt{m} n^{-\frac{c_s}{2d\gamma}}\right) = O_p\left(n^{-\frac{c_s}{2d\gamma}}\right).$$

For the local case, the weights vanish outside the kernel window by the compact support of K . Let $\mathcal{N}_h(\mathbf{x}) := \{i : K_h(\mathbf{X}_i - \mathbf{x}) \neq 0\}$; then $|\mathcal{N}_h(\mathbf{x})| = O_p(mh^p)$ by (L2). Applying Cauchy–Schwarz on this window,

$$T_1 \leq \left(\sum_{i \in \mathcal{N}_h(\mathbf{x})} \widehat{w}_i(\mathbf{x})^2 \right)^{1/2} \left(\sum_{i \in \mathcal{N}_h(\mathbf{x})} \Delta_i^2 \right)^{1/2}.$$

Standard local-linear weight bounds under (L1)–(L3) give $\sum_{i \in \mathcal{N}_h(\mathbf{x})} \widehat{w}_i(\mathbf{x})^2 = O_p((mh^p)^{-1})$, while

$$\sum_{i \in \mathcal{N}_h(\mathbf{x})} \Delta_i^2 = O_p(mh^p n^{-2c_s/(2d\gamma)})$$

Thus again $T_1 = O_p(n^{-c_s/(2d\gamma)})$.

Step 2: weight estimation term T_2 . By (G4)/(L5), $\|\mathbf{Q}_{Y_i}(t)\|_2 \leq R_{\mathcal{M}}$ a.e. t , hence $\|\mathbf{Q}_{Y_i}\|_{L^2} \leq R_{\mathcal{M}}$. Therefore

$$T_2 \leq \sum_{i=1}^m |\widehat{w}_i(\mathbf{x}) - w_i(\mathbf{x})| \|\mathbf{Q}_{Y_i}\|_{L^2} \leq R_{\mathcal{M}} \sum_{i=1}^m |\widehat{w}_i(\mathbf{x}) - w_i(\mathbf{x})|.$$

Applying Lemma 19 in the global case and Lemma 20 in the local case yields

$$T_2 = \begin{cases} O_p(\sqrt{\frac{p}{m}}), & \text{global,} \\ O_p\left(\frac{p}{\sqrt{mh^p}}\right), & \text{local.} \end{cases}$$

Step 3: oracle regression fluctuation and local bias term T_3 . *Global case.* Under (G3), $\mathbf{g}(\mathbf{x}, t)$ is affine in \mathbf{x} . Using the moment identities $\mathbb{E}[w^{(G)}(\mathbf{X}, \mathbf{x})] = 1$ and $\mathbb{E}[w^{(G)}(\mathbf{X}, \mathbf{x})(\mathbf{X} - \boldsymbol{\mu})] = \mathbf{x} - \boldsymbol{\mu}$, one checks coordinate-wise that

$$\mathbb{E}\left[w^{(G)}(\mathbf{X}, \mathbf{x}) \mathbf{Q}_Y(t)\right] = \mathbf{g}(\mathbf{x}, t), \quad \text{a.e. } t. \quad (72)$$

Thus $\widetilde{m}^{(G)}(\mathbf{x})$ is an empirical average for the target, and by the Hilbert-space CLT/variance bound,

$$T_3 = \left\| \frac{1}{m} \sum_{i=1}^m w^{(G)}(\mathbf{X}_i, \mathbf{x}) \mathbf{Q}_{Y_i} - \mathbb{E}[w^{(G)}(\mathbf{X}, \mathbf{x}) \mathbf{Q}_Y] \right\|_{L^2} = O_p\left(m^{-1/2}\right).$$

Local case. Write $\mathbf{g}(\mathbf{z}, t) = \mathbb{E}[\mathbf{Q}_Y(t) \mid \mathbf{X} = \mathbf{z}]$. A second-order Taylor expansion of $\mathbf{g}(\cdot, t)$ around \mathbf{x} , together with the local-linear moment conditions $\mathbb{E}[w^{(L)}(\mathbf{X}, \mathbf{x}; h)] = 1$ and $\mathbb{E}[w^{(L)}(\mathbf{X}, \mathbf{x}; h)(\mathbf{X} - \mathbf{x})] = \mathbf{0}$, implies (coordinate-wise) that for a.e. t ,

$$\left\| \mathbb{E}[w^{(L)}(\mathbf{X}, \mathbf{x}; h) \mathbf{Q}_Y(t)] - \mathbf{g}(\mathbf{x}, t) \right\|_2 = O(h^2).$$

Squaring and integrating over t and using (L4) yields the L^2 -bias bound

$$\left\| \mathbb{E}[w^{(L)}(\mathbf{X}, \mathbf{x}; h) \mathbf{Q}_Y] - \mathbf{g}(\mathbf{x}, \cdot) \right\|_{L^2} = O(h^2).$$

In addition, the sample fluctuation around this expectation has an effective sample size mh^p , giving

$$\left\| \mathbf{Q}_{\widetilde{m}^{(L)}(\mathbf{x})} - \mathbb{E}[w^{(L)}(\mathbf{X}, \mathbf{x}; h) \mathbf{Q}_Y] \right\|_{L^2} = O_p\left((mh^p)^{-1/2}\right),$$

so altogether

$$T_3 = O(h^2) + O_p\left((mh^p)^{-1/2}\right).$$

(Again the $(mh^p)^{-1/2}$ term is dominated by T_2 once the explicit $p/\sqrt{mh^p}$ term is tracked.)

Step 4: collect terms. Combining Steps 1–3 in (71) yields the two stated rates. ■